

RD-A154 633

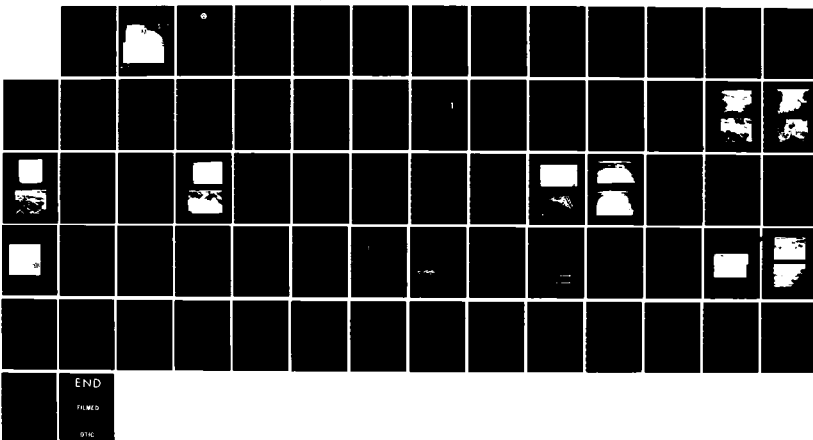
USING SHIP WAKE PATTERNS TO EVALUATE SAR (SYNTHETIC  
APERTURE RADAR) OCEAN. (U) NAVAL OCEAN SYSTEMS CENTER  
SAN DIEGO CA R R HAMMOND ET AL. FEB 85 NOSC/TR-978

1/1

UNCLASSIFIED

F/G 17/9

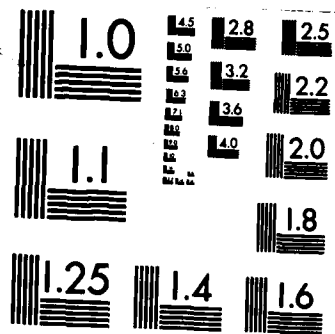
NL



END

FILED

9TC



MICROCOPY RESOLUTION TEST CHART  
NATIONAL BUREAU OF STANDARDS-1963-A

TR 978

TR 978

Technical Report 978

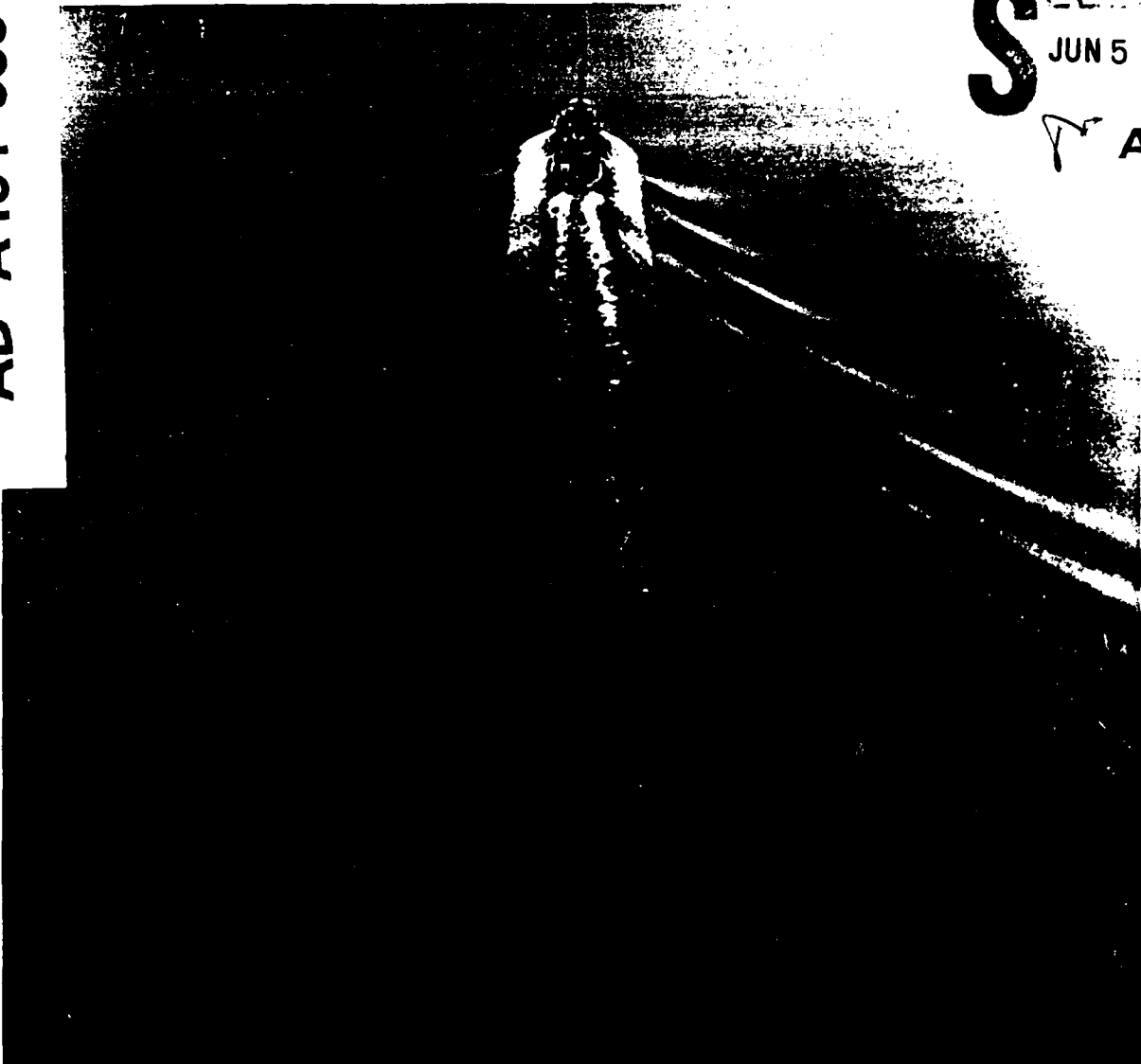
February 1985 — Interim Report

**USING SHIP WAKE PATTERNS TO EVALUATE SAR  
OCEAN WAVE IMAGING MECHANISMS**

Joint U.S.—Canadian Ocean Wave Investigation Project

R.R. Hammond, R.R. Buntzen, E.E. Floren

AD-A154 633



DTIC  
ELECTE  
S JUN 5 1985  
A

DTIC FILE COPY

**Naval Ocean Systems Center** San Diego, California 92152-5000



Approved for public release; distribution unlimited.

31 662



NAVAL OCEAN SYSTEMS CENTER SAN DIEGO, CA 92152

---

AN ACTIVITY OF THE NAVAL MATERIAL COMMAND

---

F. M. PESTORIUS, CAPT, USN

Commander

R.M. HILLYER

Technical Director

ADMINISTRATIVE INFORMATION

The work described in this report was conducted under program element 61152, project number ZR00 001, work unit ZS68 during FY 83 and FY 84 under joint sponsorship from NOSC inhouse research funds and the Office of Naval Research. Additional FY 84 work on this project for the above sponsors is underway and will be reported under separate cover upon completion.

Released by  
D. R. Wehner, Head  
Radar Systems and Technology  
Branch

Under authority of  
R. L. Petty, Head  
Electromagnetic Systems and  
Technology Division

ACKNOWLEDGMENT

Special acknowledgment is given to Dr. Blyth Hughes and the Defence Research Establishment, Pacific data collection and analysis team for their invaluable assistance throughout this effort. The surface data taken from the CFAV ENDEAVOUR in Dabob Bay contributed significantly to the NOSC Kelvin Wake Analysis effort. In addition, platform position data and airborne photography from their helicopter allowed us to more accurately select locations within the wake for more detailed analysis.

The authors would also like to thank Dr. Steve Stewart and Mr. Gary Gilbert of NOSC, and Mr. Jake Gibbs and Mr. Jon Hubbard from Computer Sciences, Corp., for their extremely valuable support during data collection and subsequent analysis effort.

UNCLASSIFIED

SECURITY CLASSIFICATION OF THIS PAGE

## REPORT DOCUMENTATION PAGE

1a. REPORT SECURITY CLASSIFICATION UNCLASSIFIED		1b. RESTRICTIVE MARKINGS	
2a. SECURITY CLASSIFICATION AUTHORITY		3. DISTRIBUTION/AVAILABILITY OF REPORT Approved for public release; distribution unlimited.	
2b. DECLASSIFICATION/DOWNGRADING SCHEDULE			
4. PERFORMING ORGANIZATION REPORT NUMBER(S) NOSC TR 978		5. MONITORING ORGANIZATION REPORT NUMBER(S)	
6a. NAME OF PERFORMING ORGANIZATION Naval Ocean Systems Center	6b. OFFICE SYMBOL (if applicable)	7a. NAME OF MONITORING ORGANIZATION	
6c. ADDRESS (City, State and ZIP Code) San Diego, CA 92152-5000		7b. ADDRESS (City, State and ZIP Code)	
8a. NAME OF FUNDING/SPONSORING ORGANIZATION Office of Naval Research	8b. OFFICE SYMBOL (if applicable)	9. PROCUREMENT INSTRUMENT IDENTIFICATION NUMBER	
8c. ADDRESS (City, State and ZIP Code) 800 N. Quincy St. Arlington, VA 22217		10. SOURCE OF FUNDING NUMBERS PROGRAM ELEMENT NO. 61152 PROJECT NO. ZR00 001 TASK NO. ZR0310304 WORK UNIT NO. 160-ZS68	
11. TITLE (include Security Classification) <b>USING SHIP WAKE PATTERNS TO EVALUATE SAR OCEAN WAVE IMAGING MECHANISMS JOINT U.S. - CANADIAN OCEAN WAVE INVESTIGATION PROJECT</b>			
12. PERSONAL AUTHORISATION R.R. Hammond, R.R. Buntzen, E.E. Floren			
13a. TYPE OF REPORT Interim	13b. TIME COVERED FROM <u>FY83</u> TO <u>FY84</u>	14. DATE OF REPORT (Year, Month, Day) February 1985	15. PAGE COUNT 64
16. SUPPLEMENTARY NOTATION			
17. COSATI CODES		18. SUBJECT TERMS (Continue on reverse if necessary and identify by block number) Synthetic aperture radar Ocean waves Wave imaging Wake patterns SEASAT	
19. ABSTRACT (Continue on reverse if necessary and identify by block number)  The Naval Ocean Systems Center (NOSC), in collaboration with the Canadian Defence Research Establishment, Pacific (DREP), conducted the Joint Ocean Wave Investigation Project (JOWIP) to evaluate the detectability of ocean wave structures on imaging synthetic aperture radar (SAR). This project made use of relatively well understood Kelvin surface ship wake patterns generated under controlled and well documented surface environmental conditions to isolate SAR image parameters.			
20. DISTRIBUTION/AVAILABILITY OF ABSTRACT <input checked="" type="checkbox"/> UNCLASSIFIED/UNLIMITED <input type="checkbox"/> SAME AS RPT <input type="checkbox"/> DTC USERS		21. ABSTRACT SECURITY CLASSIFICATION UNCLASSIFIED	
22a. NAME OF RESPONSIBLE INDIVIDUAL R.R. Hammond		22b. TELEPHONE (include Area Code) (619)225-6243	
22c. OFFICE SYMBOL Code 744		Agency Accession DN187 520	

DD FORM 1473, 84 JAN

03 APR EDITION MAY BE USED UNTIL EXHAUSTED  
ALL OTHER EDITIONS ARE OBSOLETEUNCLASSIFIED  
SECURITY CLASSIFICATION OF THIS PAGE

CONTENTS

SUMMARY . . .	page 1
BACKGROUND . . .	2
SHIP WAKES AND SAR IMAGE PARAMETERS . . .	6
Surface Wake Structures . . .	6
Internal Waves . . .	8
SAR Parameters and Image Format . . .	9
SAR IMAGE MODULATION . . .	12
Tilt Modulation . . .	13
Hydrodynamic Modulation . . .	14
Velocity Bunching . . .	15
SAR AND SURFACE TRUTH DATA OBTAINED . . .	17
SAR WAKE OBSERVATIONS . . .	21
DATA ANALYSIS AND DISCUSSION . . .	33
SAR Image Data . . .	33
SAR Wake Image Modulation Levels . . .	33
Oblique Photographic Observations of Surface Roughness . . .	37
Vertical Photography for Short Gravity Wavelength and Height Determination . . .	42
Stereo Mensurations . . .	51
Inner Wake Slope Observations . . .	55
Analysis Summary . . .	55
CONCLUSIONS AND RECOMMENDATIONS . . .	64
REFERENCES . . .	67
APPENDIX A - AVAILABLE DIGITAL DATA . . .	71
APPENDIX B - VERTICAL (STEREO) PHOTO TIMES . . .	73
APPENDIX C - DREP OBLIQUE PHOTO TIMES . . .	79

Accession #	
NTIS GRANT #	
DTIC T#	
Unannounced	
Justification	
By _____	
Distribution/	
Availability Codes	
Dist	Avail and/or Special



SUMMARY

was conducted

The Naval Ocean Systems Center (NOSC), in collaboration with the Canadian Defence Research Establishment, Pacific (DREP), conducted the Joint Ocean Wave Investigation Project (JOWIP) to evaluate the detectability of ocean wave structures on imaging synthetic aperture radar (SAR). This project used of relatively well understood Kelvin surface ship wake patterns generated under controlled and well documented surface environmental conditions to isolate SAR image parameters.

SEASAT SAR images of the ocean surface established the importance of wakes in ship surveillance from space. The use of waves of known wavelength and direction provide the opportunity to evaluate the SAR contribution to ocean wave forecasting. Airborne SAR operated by the Canadian Centre for Remote Sensing (CCRS) gathered the doppler histories and high resolution images were generated by the Environmental Research Institute of Michigan (ERIM).

SEASAT-like images made with L-band SAR are presented: (1) to suggest how ship-generated surface roughness combines with the velocity-bunching mechanism in calm ocean areas to produce the unusually narrow wakes observed for azimuth-traveling ships on SEASAT images; and (2) to estimate conditions under which SAR image modulation mechanisms can be expected to produce wake images.

A method is described for using the Kelvin transverse ship wake wave component to quantitatively evaluate the contributions of various SAR ocean wave imaging mechanisms. It makes use of the narrow sector of surface roughness generated by a ship along its track to produce SAR images of the longest waves in its wake system on flat calm water. By varying ship headings and speeds, relative SAR image modulation mechanisms can be quantitatively evaluated as a function of surface wave propagation direction, wavelength, radar incidence angle, and to some extent, height. Under near zero local wind conditions, ship-induced roughness may also be used to determine ocean swell conditions.

## BACKGROUND

The existence of ship wakes on SEASAT SAR images has been discussed by multiple authors (Fu and Holt, 1982; Vesey and Stewart, 1982), and the use of Kelvin surface wake components for investigating surface wave SAR image modulation mechanisms has been pursued by NOSC for several years (Hammond, et al., 1983). One area of specific interest has been the narrow wake angles observed on many SEASAT images. Suggested responsible mechanisms for these narrow wake images include (1) increased radar roughness associated with ship-generated surface wavelengths near the Bragg reinforcement length ( $\approx 30$  cm for SEASAT); (2) enhanced slopes associated with these shorter wavelengths; (3) the surface manifestations of ship-generated internal waves; or (4) some combination of the above. Controversy over wakes is inevitable when we try to explain specific wave observations with imaging theory derived with statistical ensemble characteristics as variables. The application of SAR to naval ocean surveillance missions requires detailed understanding of both discrete wake patterns and statistical wave ensembles.

A SEASAT SAR data base including 49 ship wakes over the full range of ship headings was compiled from JPL images which were processed digitally and optically. This data base produced the statistics shown in table 1 as a function of ship track orientation relative to the SAR track. It should be pointed out that an estimate of ships heading was prerequisite for inclusion in this data base. Because the resolution of these images varied from 25 to 40 meters and the longest wave in a "typical" (Webster, 1982) 15-knot ship wake is only 38 meters the expected wake image included only the common Kelvin wake envelope arms at approximately +19.5 degrees and perhaps an elongated turbulent patch extending for some distance directly aft of the ship.

Table 1. SEASAT ship wake image data summary.

Ship-Track Orientation rel to SAR track	Ship Sample	Ships Without Wake Arms		Ships with One Wake Arm		Ships with Two Wake Arms		Total Wake Arms	
		No.	%	No.	%	No.	%	No.	%
0 - 14°	19 39	8	47	6	30	5	42	16	36
15 - 29°	10 20	1	6	5	25	4	33	13	30
30 - 44°	9 18	1	6	5	25	3	25	11	25
45 - 59°	4 8	2	12	2	10	-	-	2	5
60 - 74°	5 10	3	18	2	10	-	-	2	5
75 - 90°	2 4	2	12	-	-	-	-	-	-
49 ships		17	(35%)	20	(41%)	12	(24%)	44 arms	

While each of the 49 ships could display some combination of these three features, table 1 indicates that 35 percent of the ships displayed neither port nor starboard envelope arms. The turbulent wake, usually an absence of radar return against a saturated background, was the most prevalent and surprisingly persistent wake feature averaging 8 km long. The turbulent wake was the only feature observed for ships traveling in the radar range direction. As ships headings became more along track, wake arms began to appear, usually with the radar range traveling wake component side of the wake first, and both sides become increasingly common as the relative track orientation angle approached zero. Wake arms averaged 5 km long on SEASAT images but their included angles varied widely from the expected +19.5-degree angle associated with the Kelvin envelope where the highest amplitude waves are known to be located (Inui, 1962).

The distribution of observed wake half-angles (each side considered separately) displayed the two distinct modes shown in figure 1. The upper mode peaks near the anticipated Kelvin envelope angle, but a second unexpected peak near 3 degrees is also a dominant feature.

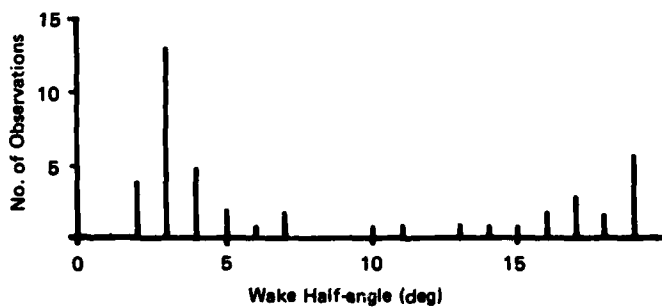


Figure 1. Observed distribution of SEASAT ship wake angles.

During high surface winds with highly nonlinear imaging conditions (Alpers, 1983), no wake features were observed. With lower winds the turbulent wake appears first as a reduced radar return against a saturated background. As wind speed approaches the linear imaging regime ( $\approx 3.6$  m/s for SEASAT with four resolution cells per ocean wavelength [Vesecky, et al., 1982]), smeared lines may appear on high resolution images along the Kelvin envelope arms (range-traveling arm first) and both arms may become apparent for range-traveling ships where the wake component waves propagate in the linear SAR modulation domain (Alpers et al., 1981). At still lower wind speeds there is insufficient radar cross-section  $\langle\sigma_0\rangle$  for the wake component waves to modulate the image and these waves gradually disappear (upper mode in figure 1) and are replaced by the narrow wake (lower mode). We hypothesized these smaller observed wake angles were

- (1) dependent on short gravity wave surface roughness generated by the ship, and
- (2) observable only under relatively calm local wind conditions.

During the summer of 1983, the Naval Ocean Systems Center (NOSC) in conjunction with the Canadian Defence Research Establishment, Pacific (DREP) embarked on a joint project to observe ship wake structures.

The U.S. Navy's objectives in the U.S./Canadian Joint Ocean Wave Investigation Project (JOWIP) were to

- (1) resolve the narrow wake image controversy
- (2) test ocean surface wave imaging theories using the well known components of the Kelvin wake pattern
- (3) evaluate SAR detection of ship-generated internal waves (IW) relative to naturally occurring IW patterns.

DREP, which is a highly capable Canadian Forces laboratory in Esquimalt, British Columbia, shares similar interests with NOSC. Because of this and DREP's considerable experience with ship-generated internal waves and access to the Canadian Centre for Remote Sensing (CCRS) airborne simultaneous dual polarization X-L band SAR, a joint venture sharing the surface truth collection burden, instruments, and data seemed appropriate to SAR imaging problems.

One serious problem in any type of SAR evaluation has been the paucity of image data obtainable for the multitude of uncontrollable environmental, flight, and radar variables involved. Our plan was to concentrate on the SEASAT parameters (L-band, horizontally polarized,  $\sim 23^\circ$  surface incidence angle) and obtain high confidence data on a restricted set of variables before extending the cases to be considered.

Since statistical description of the ocean surface waves injects large uncertainties, we used the relatively well known wavelengths and propagation directions within the Kelvin surface wake of a large dedicated U.S. Navy ocean tug. The plan called for demonstrating reproducible results under conditions critical for verification of current image modulation theory; first, on flat calm waters where the scattering waves would be generated by the ship and second, on a modestly wind-roughened surface where background waves would pose minimum interference in resolving the longer ship wake components. The ship was to travel (1) in the same direction as the radar orienting its shorter wake components in the radar's range direction, the situation which produced narrow wake angles on SEASAT images; and (2) perpendicular to the radar track to orient the longer wake wavelengths in the range direction.

In order to separate surface and internal wave effects it became necessary to operate in two separate areas sheltered from wind and swell as much as possible — a primary location with as little stratification as possible, and the other location highly stratified. Choice of actual areas involved tradeoffs against ship transit times, Canadian aircraft flight times, and basing requirements as well as local wind, swell, and internal wave

conditions. After all factors were considered, we selected our primary sites in the NUWES range in Dabob Bay, Washington and a very highly stratified location in Knight Inlet in British Columbia. Surface ship wake tests were conducted in Dabob Bay between 26-28 July, and the IW generation tests were conducted in Knight Inlet on 2-3 August 1983.

The surface wave experiments involved higher speed (12-16 knots) ship runs on Dabob Bay. Results of these tests are reported here by NOSC and the results of the ship-generated and natural internal wave observations will be prepared by DREP. Ship-generated internal waves were produced by both the USS QUAPAW and CFAV ENDEAVOUR running at 1-5 knots in the highly stratified waters of Knight Inlet. The SAR images of these wakes revealed weak, dark (absence of return) lines against a wind-roughened surface. No corresponding subsurface evidence of internal wave wake activity was detected on Dabob Bay during repeated CFAV ENDEAVOUR echosounder passes through the QUAPAW wake system (Hughes, 1983). As will be seen later, the absence of wind roughening during the Dabob SAR runs, which resulted in narrow wake images, removed the SAR clutter background against which internal waves are normally seen.

The Canadian Centre for Remote Sensing aircraft SAR flew 15 passes over the Dabob location with the US Navy ocean tug (USS QUAPAW) laying down wake patterns. The Canadian oceanography ship, CFAV ENDEAVOUR, collected wind and surface wave height/slope data. A stereo-photo fixed-wing aircraft and a helicopter recorded the events on vertical and oblique photographs, respectively. The SAR imaging geometry was held as close as possible to that of SEASAT, with primary emphasis on L-band HH polarization, and the image times were selected to the maximum extent possible for wind and wave conditions. The CCRS/ERIM SAR produces slant range and azimuth resolutions of 3 and 5 meters, respectively, for stationary targets using a coherent integration time of 1.4 seconds. Even after translation to the ground plane and correction for motion-induced image smear, a 16-meter maximum effective resolution was achieved when estimated by the equations of Alpers et al., (1981). It was hoped that this SAR would resolve the longer transverse waves ( $\approx 38$  m) in a 15-knot ship wake under proper surface conditions using the effective resolution cells per ocean wavelength ( $n_e > 2$ ) criterion of Veseyky, et al; 1982.

## SHIP WAKES AND SAR IMAGE PARAMETERS

The following brief background on ship wake structures and SAR imaging geometry will provide the basic equations and parameters needed for the analysis which follows.

### SURFACE WAKE STRUCTURES

A ship's hull imparts velocity to the water at all angles between 0 and 90 degrees to the ship track. The initial amplitudes depend on the shape of the hull but outside the immediate disturbance area the resulting "free waves" of wavelength ( $\lambda$ ) and velocity ( $c$ ), propagating in any direction ( $\alpha$ ) are related to the ship's speed ( $V$ ) (Havelock, 1934) by:

$$\alpha = \cos^{-1} C/V \quad (1)$$

$$\lambda(\alpha) = \frac{2\pi}{g} V^2 \cos^2 \alpha \quad (2)$$

We may summarize the velocity vectors originating from a ship at point P as shown in figure 2.

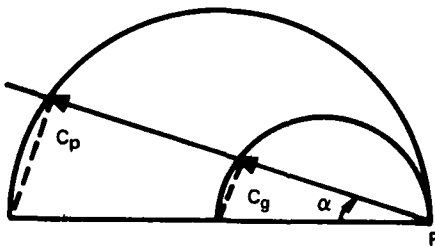


Figure 2. Wake velocity vectors as a function of propagating angle ( $\alpha$ ).

The energy of the waves in direction  $\alpha$  originating at point P with phase velocity  $C_p$  will propagate with group velocity  $C_g = C_p/2$  as indicated by the smaller semicircle in figure 2. Note that although the deep water wave velocity ( $C_p = \sqrt{g\lambda/2\pi}$ ) will depend on ship speed ( $V$ ), the ratio  $C_p/V$  for any specific  $\alpha$  is constant. This constant expansion rate agrees with our observation that ship wake structures expanding in the cross track direction appear stationary with respect to the ship in photographic and SAR images.

Since the common measurable parameters on ship wake images are (1) the ship heading ( $H_0$ ), (2) the vee-angle or commonly half vee-angle ( $\theta_0$ ), and (3) one or two wake envelope arm lengths, it is advantageous to express wake

component parameters for all points ( $Q$ ) within the envelope arms in terms of the polar coordinates ( $\theta, R$ ) with origin approximately at the ship as shown in figure 3.

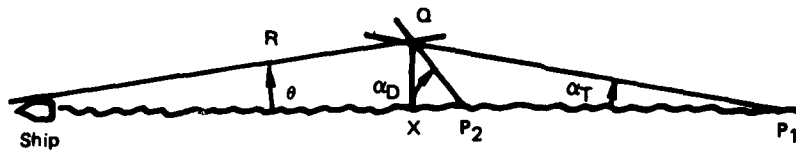


Figure 3. Wake envelope coordinates ( $X, \theta$ ).

This geometry allows the solution for wake coordinate  $\theta$  in terms of propagation directions ( $\alpha$ ) independent of ship speed and hull shape, as given by equation (3) which associates two propagation directions ( $\alpha$ ) with each observed wake coordinate angle ( $\theta_0$ ).

$$\alpha = \arctan \left[ \frac{1 \pm (1 - 8 \tan^2 \theta)}{4 \tan \theta} \right] \quad (3)$$

The longer wavelength Kelvin wave components, which move more or less in the direction of ship, are termed transverse ( $\alpha_T < 35^\circ$ ) and those more or less crosstrack propagating waves ( $35^\circ < \alpha_D < 90^\circ$ ) are termed divergent. Havelock (1934), Inui (1962), and Lighthill (1978) in their pioneering work on the wave resistance of ships, have shown that it is possible to obtain a good approximation to surface wake amplitude  $A(X, \theta)$  for any point in the wake in terms of a linear combination of the amplitudes  $A_T(\alpha_T)$  and  $A_D(\alpha_D)$  corresponding to these two "elementary waves." This method is applicable to the entire range of ocean vessels, Froude numbers  $= V/\sqrt{gL} < 0.35$  (Inui, 1962), for locations further than several ship lengths aft. Variations of these equations can accommodate all points within the outer edge of the Kelvin vee-wake pattern ( $\theta = 19.5^\circ$ ,  $\alpha = 35^\circ$ ) where the familiar larger amplitude visible "cusp" waves mark the transition between transverse and divergent wake components.

Assuming that the SAR wake pattern on a flat uniformly Bragg roughened surface results from surface wake disturbances, the wavelengths, propagation

directions, amplitudes, and resulting slopes can be obtained for resolution elements along any observed wake arm ( $\theta = \theta_0$ ). Propagation directions ( $\alpha$ ) for a common SAR image wake coordinate ( $\theta_0 = 3.5^\circ$ ) are  $\alpha_T = 3.5^\circ$  and  $\alpha_D = 83^\circ$ . The corresponding wavelengths for the transverse ( $\alpha_T = 3.5^\circ$ ) and divergent ( $\alpha_D = 83^\circ$ ) components are shown in table 2 for various ship speeds.

Table 2. Surface ship wake component wavelengths along the  $\theta_0 = 3.5^\circ$  wake coordinate angle for various ship speeds

<u>Ship Speed (knots)</u>	<u>10</u>	<u>12</u>	<u>13</u>	<u>14</u>	<u>15</u>
Divergent Wavelength (m)	0.25	0.37	0.43	0.50	0.57
Transverse Wavelength (m)	16.9	24.4	28.6	32.2	38.1

JOWIP ship-wake-component amplitudes several ship lengths aft were estimated to be between 5 and 25 centimeters before the experiment. For planning purposes, we used 10 centimeters 1000 meters aft. Preliminary stereo photographic measurements and shipboard wave height time series data have confirmed this but precise variation with propagation direction remains to be extracted from wake photography. The length of time that short gravity divergent waves ( $\sim 30$  cm) could survive in the open ocean is another area of uncertainty. In calm ocean areas, where the population of wind-generated short wavelengths is depleted and strong interactions minimized, something like the 10-minute energy e-folding time estimated for viscous damping (Lighthill, 1978) might be appropriate. Even this short interval could yield a 4.5-kilometer wake for a 15-knot ship.

#### INTERNAL WAVES

Since the separation of Kelvin wake and internal wave effects on SAR images is the primary objective of the NOSC part of the JOWIP experiment, it was desirable to choose a measurement site where surface ships were not able to produce internal waves. Depending principally on ship speed and density structure of the water column, two distinct physical mechanisms associated with surface ship motion are capable of generating internal wave wakes: water vertical displacement by the hull and collapse of the turbulent wake.

Hull-induced internal waves having wavelengths near the ship length can be significant if the ship speed is matched to their phase velocity in the medium. This phase velocity is given by a dispersion relationship which depends on the density gradient in the water column. These waves also exhibit a maximum frequency which is given by the quantity known as the Brunt-Vaisala frequency ( $N(z)$ ).

$$N(z) = \left[ \frac{g}{\rho(z)} \frac{d\rho(z)}{dz} \right]^{1/2} \text{ radians sec}^{-1}. \quad (4)$$

SAR TRACK



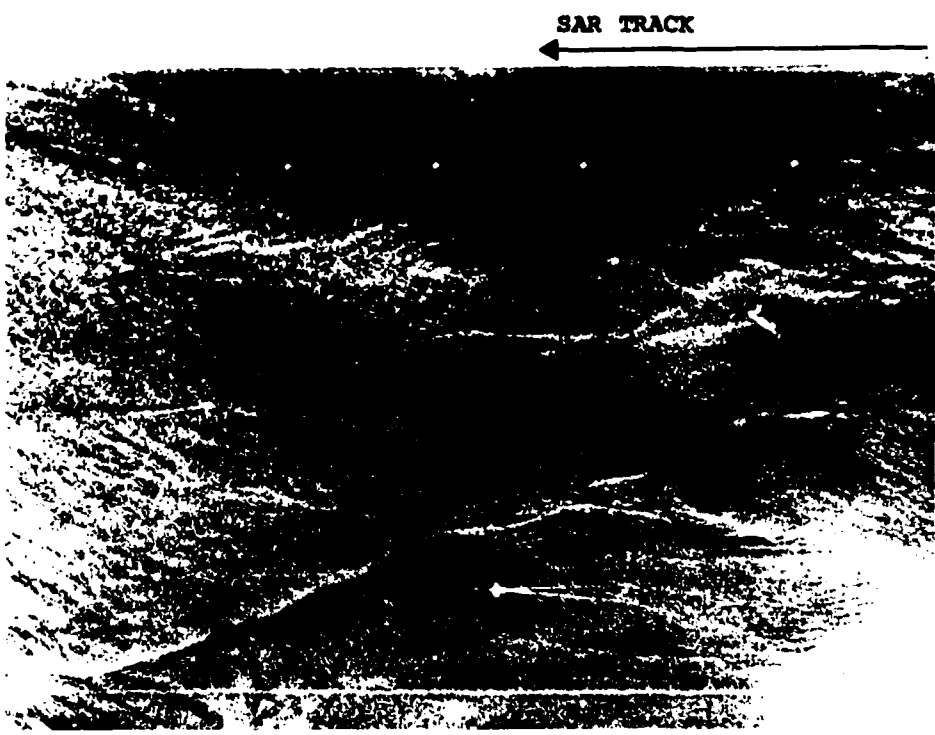
A. SEASAT SAR Rev 1368-1, 30 Sept 1978, 15:58:30 GMT

SAR TRACK

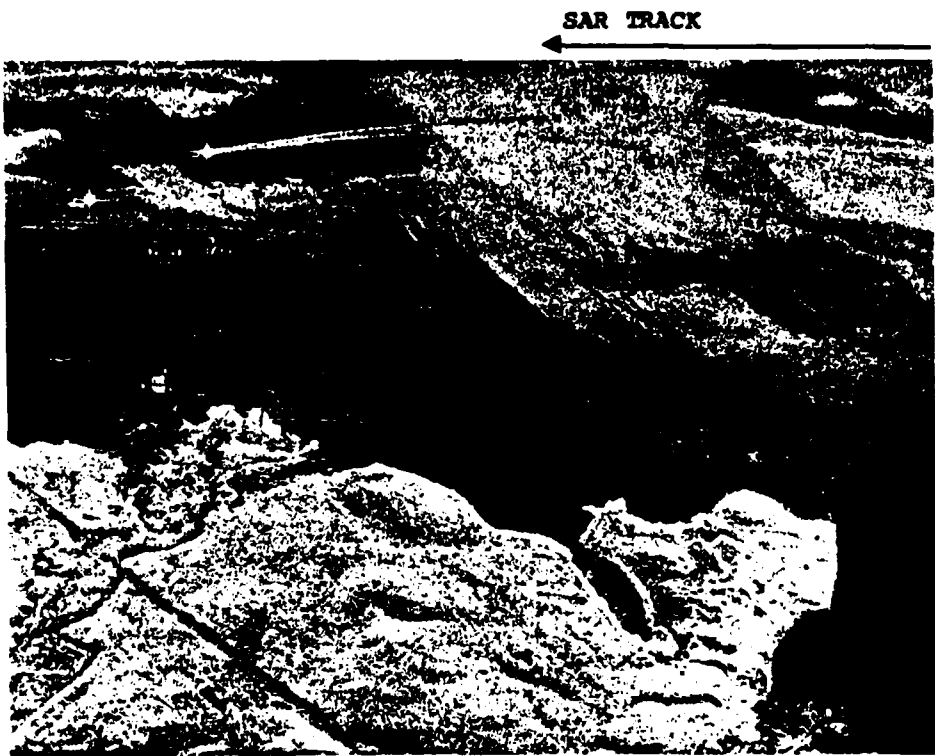


B. JOWIP SAR Flight 1, Pass 4, 23 July 1983, 18:53:56 PDT

Figure 11. Oblique-traveling ship wake comparison.



A. SEASAT SAR Rev 407-2, 25 July 1978, 11:18:50 GMT



B. JOWIP SAR Flight 8, Pass 2, 18 July 1983, 08:16:09 PDT

Figure 10. Azimuth-traveling ship wake comparison.

## SAR WAKE OBSERVATIONS

Figures 10, 11, and 12 show representative comparisons between SEASAT and the CCRS/ERIM SAR wake images for azimuth-, oblique-, and range-traveling ships. For the JOWIP L-band SAR, strong narrow wake modulations were observed as expected for azimuth-traveling ships under low wind conditions ( $\sim 2.0$  m/s). Comparison with SEASAT generally showed similar backgrounds, contrasts, and wake angles. Inner wake detail is usually absent from SEASAT images because wake wavelengths ( $\sim 40$  m) are short when compared to the processed resolutions ( $\sim 25$  m). Wake angles for most of the CCRS/ERIM SAR images appear narrower because these optically correlated images are in the slant rather than the ground range plane.

In order to resolve ship wake angles on SAR images, the wake arm must exceed the theoretical minimum lengths shown in table 7. The lengths are based on only one resolution cell between the wake centerline and the wake arm, ideal SAR performance, and no error in measurement. Note how the higher JOWIP range resolution reduces the required wake lengths. From the first two entries in table 7 it is apparent that wake angle measurement errors of 0.5 to 1 degree are to be expected (observed wake arm lengths roughly 2 and 7 km in figure 10) even under ideal conditions.

Table 7. Minimum wake arm lengths for SAR  
wake angle measurements (23° incidence).

Wake Half Angle $\theta_0$ (deg)	JOWIP (km)	SEASAT (km)	CV 990 (km)
0.5	1.84	5.75	4.83
1.0	0.92	2.88	2.42
1.5	0.61	1.90	1.60
2.0	0.46	1.43	1.20
2.5	0.37	1.15	0.97
3.0	0.31	0.95	0.80
3.5	0.27	0.83	0.70
4.0	0.23	0.73	0.61

In the upper SEASAT image in figure 10A for azimuth traveling ships, wake angles for the bottom center wake measured between 3 and 4 degrees. In the slightly wind-roughened area half way up the image, one wake arm (probably upwind) is missing. The lower CCRS/ERIM image (figure 10B) shows a combination sequence where the positive return wake arms disappear almost immediately and are replaced by a dark (absence of return) linear scar where the ship passed through the locally wind-roughened water surface area. This wind roughening was simultaneously recorded photographically and is estimated to correspond to wave amplitudes of a few centimeters. The wake modulation is

Table 6. Dabob Bay surface wind summary.

SAR Flt-Pas (number)	Time Interval	Speed (m/s)	Direction (°T)	Time Interval (PDT)	Speed (m/s)	Direction (°T)
1-4	No data available					
5-3	1024-1025	5.1 $\pm$ 0.3	186-220	1025-1031	5.8 $\pm$ 0.5	193-219
5-4	1103-1108	7.7	205			
6-1	1518-1523	6.0	210			
6-4	1643-1648	6.4 $\pm$ 0.9	180-199	1652-1658	5.3 $\pm$ 0.5	180-219
7-1	1605-1610	11.2	235			
7-3	1706-1711	9.7	230			
7-5	1822-1826	7.0	235			
7-7	1932-1937	6.5	235			
8-1	0724-0727	2.2 $\pm$ 0.2	239-253	0735-0739:40	1.8 $\pm$ 0.1	214-240
8-2	0812-0817	1.5 $\pm$ 0.3	180-230	0819-0826:30	2.0 $\pm$ 0.1	180-216
8-3	0859-0904	2.5 $\pm$ 0.3	189-206	0906-0910:20	2.8 $\pm$ 0.2	188-204
8-4	0943-0948	2.5 $\pm$ 0.3	191-226	0944-0955:30	2.0 $\pm$ 0.2	198-224
9-1	1313-1317	<1	SW	1317-1324	<1	SW
9-2	1353:30-1354:30	<1	SW	1356-1401:10	<1	SW
9-3	1442-1447	<2	SW	1449-1445:15	<2	SW

NOTES:

Referenced to 10 meters above surface

Entries where the ENDEAVOUR wake sampling interval is omitted are rough estimates since digital records have not been processed.

Threshold problems for very low speed.

Table 5. JONIP data inventory.

DATE 1983	SAR Run	QUAPAW		QUAPAW		SAR Image Time	Aircraft Heading	DREP Digital Data		Oblique Photo		Vertical Photo (Number of stereo pairs)
		Flt - Pass	Wake Run	Speed-Heading	Trees			(PDT)	(PDT)	Background Times	Wake Sampling Times	
		(as <sup>-1</sup> )	(°T)	(as <sup>-1</sup> )	(°T)	(PDT)	(PDT)	(PDT)	(PDT)	(PDT)	(PDT)	-
7-23	1-4D	Wake of unknown ship		01:53:56		196	None					None
7-26	5-3D	6.58 - 353	1010-1021	10:17:51	0	1024-1025	1024-1031			0		12
5-4	6.5 - 358	1055-1109	11:01:44	0	Not Processed	0	0			0		60
6-1	6.5 - 000	1509-1524	15:14:32	0	Not Processed	49	49			20		20
6-4D	6.49 - 003	1639-1653	16:44:55	0	1643-1648	1652-1658	63			45		45
7-27	7-1	6.5 - 001	1607-1621	16:18:54	90	Not Processed	24			24		30
7-3	6.5 - 343	1707-1720	17:14:49	90	Not Processed	44	44			39		39
7-5	6.5 - 347	1817-1830	18:26:41	0	Not Processed	65	65			49		49
7-7	6.5 - 347	1927-1939	19:36:40	0	Not Processed	14	14			32		32
7-28	8-1	6.40 - 346	0722-0733	07:30:44	0	0724-0727	0735-0739:40			31		4
8-2D	8.02 - 347	0808-0820	08:16:09	0	0812-0817	0819-0826:30	34			25		25
8-3D	7.90 - 349	0853-0906	09:01:18	0	0859-0904	0906-0910:20	44			26		26
8-4	7.97 - 347	0938-0949	09:47:04	0	0943-0948	0949-0955:30	42			43		43
9-1	7.92 - 76	1308-1317	13:16:13	91	1313-1317	1317-1324	34			66C		66C
9-2D	8.14 - 170	1351-1401	14:00:48	0	1353:30-1354:30	1356-1401:10	45			16		16
9-3D	8.0 - 348	1437-1449	14:46:22	0	1442-1447	1449-1454:15	78			51		51

D - Digital ground plane corrected image available

C - Single color camera from 750-foot altitude

## SAR AND SURFACE TRUTH DATA OBTAINED

During the 3 days of the surface ship wake phase of the experiment, SAR coverage of Dabob Bay produced 15 SAR images during the time intervals and with the ship speeds and headings summarized in table 5. The intended ship speed was 12 knots through run 8-1 when it was increased to 15 knots. The ship speed entries in table 5 are presented to one decimal place where they are estimated and to two decimal places in the cases where they are accurately known.

The SAR image times were coordinated to fall within the interval of the QUAPAW high speed run as shown. Most of the runs were made with both QUAPAW and the SAR aircraft on south to north tracks. Notable exceptions to this were passes 7-1, 7-3, and 9-1 with perpendicular tracks and pass 9-2 where the platforms ran in opposite directions. The SAR image from pass 1-4 was collected during a SAR pass over the SAR calibration area and surface truth is not available.

An attempt was made to compile data for each selected SAR image for a 5-minute background interval as well as during the time the DREP-instrumented CFAV ENDEAVOUR traversed the wake pattern. The surface data taken by DREP from the CFAV ENDEAVOUR includes extensive records of wind, wave height, wake slope, echo-sounder, CTD profiles, and precise (approx  $\pm$  2 meter) latitude-longitude tracks of QUAPAW, ENDEAVOUR and Cessna vertical photo aircraft. The bulk of this time series data is available on VAX/VMS 1600 BPI 9-track computer compatible digital tapes prepared by DREP and is available through NOSC. These data have been carefully corrected to geocoordinates, calibrated, and extensively cross checked. Appendix A summarizes the available digital data.

Appendix B summarizes the times that vertical photographs were taken within the wake system. Wake coordinates associated with each of these exposures are being determined from the DREP digital positioning data before selecting specific frames for analysis. Resolution from synchronized stereo pairs were used to take vertical photographs throughout the wake system to measure the lengths and heights of the anticipated short gravity waves. The fixed baseline stereo images are on 70 mm film, nominally 60 meters square with 75 percent overlap and 2 cm ground resolution. A selected example (run 8-3) where rough track reconstruction could be made from known objects included in the images will be used in the analysis presented here.

Appendix C provides the times associated with 70 mm oblique photos taken by a roving helicopter from approximately 100 feet throughout the experiment. The photographs, which provide some of the best qualitative estimates of the overall surface roughness patterns in the SAR images, will also be used in the data analysis.

Because of its critical importance to water surface radar scattering, background winds are presented in table 6 for the time intervals and SAR images shown.

With this background information it is now possible to summarize pertinent observations in the SAR images obtained.

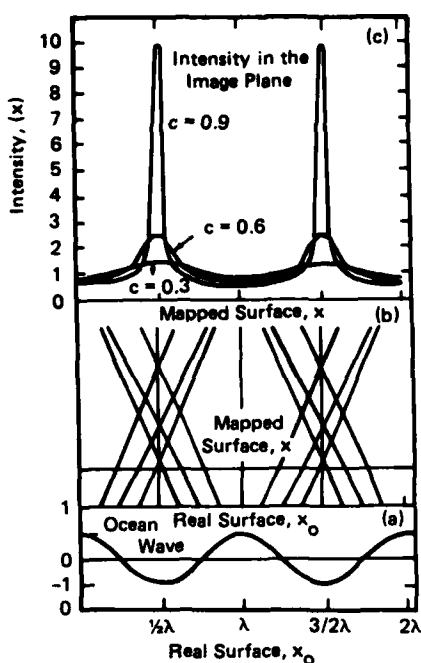


**Figure 8. Velocity bunching.**  
 (a) Surface elevation associated with ocean wave traveling in azimuthal direction. (b) Azimuthal shift of scatters in image plane.  $x_0$  is azimuthal axis on real surface and  $x$  on mapped surface, i.e., in image plane. Shift  $x - x_0$  is given by velocity of scatterers in range direction. (c) Relative power (intensity) per azimuthal resolution cell as function of azimuthal position  $x$  for different values of  $c$  defined by equation (11) (after Alpers and Rufenach, 1979)

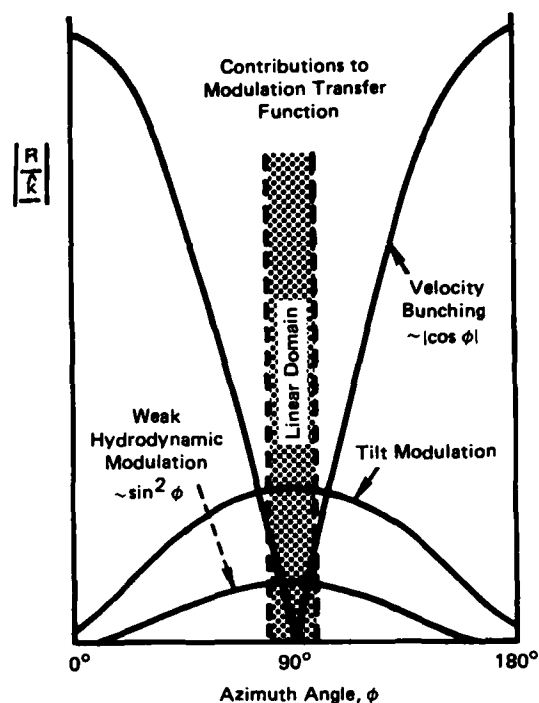


**Figure 9. The dependence of non-dimensional modulation transfer functions describing tilt, weak hydrodynamic, and velocity bunching modulation on azimuthal angle (after Alpers et al., 1981).**

**Table 4. Estimated maximum crest-to-trough image modulation.**

SAR Platform	SEASAT ( $\lambda = 100$ m, $A = 0.5$ m)		JOWIP ( $\lambda = 35$ m, $A = 0.1$ m)	
Ship Travel	Range	Azimuth	Range	Azimuth
Tilt	2.4 dB	0.2 dB	1.4 dB	0.1 dB
Hydrodynamic	1.1	0.0	0.7	0.0
Velocity Bunching	0.0	11.0	0.0	7.1

$$R(K) = -4.5 K \omega \left[ \frac{\omega - i\mu}{\omega^2 + \mu^2} \right] \sin^2 \theta, \quad (10)$$

where  $\mu^{-1}$  is termed the relaxation time constant. Following standard practice, we let  $\mu = 0$  and estimate the maximum RCS modulation contribution as  $\Delta\sigma = \langle \sigma \rangle [1 + 4.5 K A] \sin^2 \theta$  (Vesecky and Stewart, 1982). For the above cases of 100-meter and 35-meter range-traveling waves, this gives a maximum crest-to-trough modulation of 1.1 dB and 0.7 dB, respectively. The first order estimated hydrodynamic modulation is zero for all azimuth-traveling waves ( $\theta = 0$ ). Since magnitudes given by equation (10) are thought to be low (Wright et al., 1980), additional effects such as nonlinear wave interactions or other scattering mechanisms need to be investigated.

#### VELOCITY BUNCHING

When long wave orbital motions have spatially varying radial velocities, the doppler coordinate is misaddressed causing nonuniform azimuth ( $X$ ) displacement of scattering elements in the image plane. This occurs for uniformly roughened surfaces independently of other RCS modulation mechanisms and can accentuate or even introduce fictitious wavelengths. To linearly map wave fields into SAR images and preserve ocean wave spectra requires (Alpers and Rufenach, 1979) that,

$$C = |R_{VB}| A < 0.3, \quad (11)$$

where

$$|R_{VB}| = (R/V)K \omega \cos \theta g(\theta, \phi) \quad (12)$$

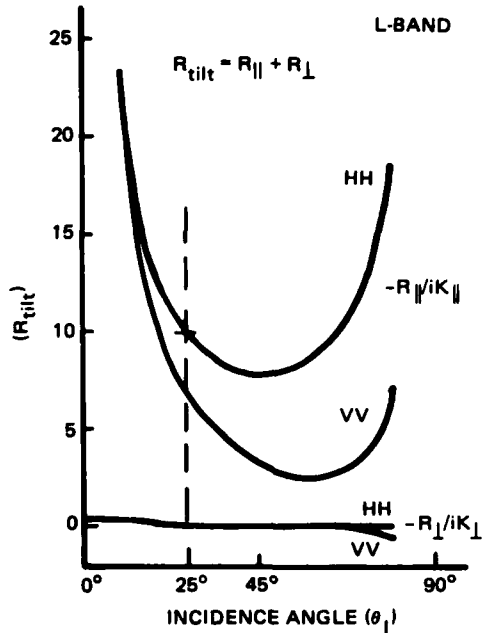
$$g(\theta, \phi) = \left[ (\sin \theta \sin \phi)^2 + \cos^2 \theta \right]^{1/2}. \quad (13)$$

As indicated by Alpers and Rufenach (1979), the effect of nonlinearity can be to enhance periodic image intensity (i.e., accentuate wavelengths) as shown in figure 8, but extreme care must be taken since this accentuation will be displaced in azimuth and phase.

For azimuth-traveling waves ( $\theta = 0$ ) and the previously selected examples, the maximum peak-to-trough modulation is estimated ( $\Delta\sigma = \langle \sigma \rangle 1 + C$ ) as 11 dB for SEASAT ( $\lambda = 100$  m,  $A = 0.5$  m) and 7.1 dB for JOWIP ( $\lambda = 35$  m,  $A = 0.1$  m). The corresponding values of the linearity parameter are  $C = 2.7$  and  $C = 1.1$ , respectively. Figure 9 summarizes the relative variation of three image-modulation transfer functions with long wave propagation direction. Table 4 assembles the maximum crest-to-trough RCS values calculated above for easy comparison. Note that these maximum values were calculated using absolute values of the complex FFTs; they cannot be easily combined.

to resolve at 25 meters although line enhancement might adequately define elongated wave crests.

Figure 7. Modulation transfer function  $R_{\text{tilt}}$  for the tilt mechanism as a function of incidence angle  $\theta_I$  for HH and VV polarization. The upper curves ( $\sim R_{\parallel}/iK_{\parallel}$ ) apply to range-traveling waves and the lower curves are for azimuth-traveling waves. These calculations apply to an L-band radar as used for SEASAT SAR. The SEASAT SAR angle of incidence  $\theta = 23^{\circ}$  (adapted from Alpers et al., 1981).



For the JOWIP radar, the estimated tilt modulation for an  $A = 0.1$  m,  $K = 2\pi/35 = 0.18$  range-traveling wave would be  $\Delta\sigma = \langle\sigma_0\rangle [1 \pm 1.8(0.1)]$ , which corresponds to a maximum tilt modulation of 1.4 dB crest-to-trough.

For azimuth-traveling ships, the estimated modulations are too small to be important; 0.2 dB and 0.1 dB for the SEASAT and JOWIP cases, respectively, which is below the expected coherent speckle level ( $\sim 0.5$  dB). For a ship heading at an angle of 55 degrees relative to the SAR track, the range traveling side of the wake envelope ( $\alpha = 35^{\circ}$ ) should display a much sharper tilt modulation than the opposite wake arm (Kelvin envelope propagation direction = ship heading  $\pm 35^{\circ}$ ).

#### HYDRODYNAMIC MODULATION

In the first order theory for decimeter waves (Alpers et al., 1981), modulation results from purely hydrodynamic interactions between the short Bragg scattering waves and the longer ocean wavelengths. Nonuniform wave-induced airflow is neglected. When the spectrum of short surface waves is assumed to be a Phillips spectrum ( $E \sim |K|^{-4}$ ), and the Bragg resonant wavelength ( $\bar{K}$ ) is taken to be in the range direction, the MTF can be written in terms of the angle ( $\theta$ ) between the long wave ( $\bar{K}$ ) and the SAR ground track (Alpers et al., 1981),

$$\sigma = \sigma_0 + \delta_\sigma = \sigma_0 \left[ 1 + \int [R(K) Z(K) e^{i(\bar{K}x - \bar{w}t)} + CC] dK \right], \quad (5)$$

where

$$R(K) = R(K)_{\text{tilt}} + R(K)_{\text{Hydro}} + R(K)_{\text{Vel Bunching}}. \quad (6)$$

The complex modulation transfer function (MTF),  $R(K)$ , includes the combined effects of the three mechanisms mentioned above. Here  $\sigma_0$  is the cross-section associated with local surface roughness;  $Z(K)$  is the Fourier transform of the amplitude ( $A$ ) of the ocean surface;  $K$  and  $w$  are wave vectors and radian frequencies of the large scale wave field; and CC is the complex conjugate.

If only one long wave ( $K$ ) is presented and the linearity conditions to be discussed below are met, then this expression can be simplified to read

$$\sigma = \sigma_0 \left[ 1 + R_K \cdot A_K \cos (Kx - wt + \delta) \right] \quad (7)$$

with

$$\delta = \tan^{-1} \left[ \frac{\text{Im } R}{\text{Re } R} \right] \quad (8)$$

$$R_K = R_{\text{tilt}} + R_{\text{Hydro}} + R_{\text{Vel Bunching}}, \quad (9)$$

facilitating meaningful comparison of the individual MTF's summarized below for specific wave directions and amplitudes.

#### TILT MODULATION

Assuming a uniformly wind-roughened surface, the effect of slope variations at different locations along the long wave gives rise to the theoretical MTF estimates in figure 7 (Vesecky and Stewart (1982)). The two parts of  $R_{\text{tilt}}$ ,  $R_{\parallel}$  and  $R_{\perp}$ , refer to tilt components in and perpendicular to the plane of incidence. For SEASAT/JOWIP incidence of 23 degrees, we have for range-traveling waves ( $\phi = 0^\circ$ ),  $R_{\text{tilt}} \approx R_{\parallel} \approx 10 K$ ; and for azimuth-traveling waves  $R_{\text{tilt}} \approx R_{\perp} \approx 0.6 K$ . The maximum modulation occurs for waves propagating in the range direction.

For SEASAT, the estimated maximum tilt cross-section modulation for an  $A = 0.5$  meter,  $K = 2\pi/100 = 0.06$  range-traveling wave would be  $\Delta\sigma = \langle \sigma_0 \rangle [1 \pm R_{\text{tilt}} A] = \langle \sigma_0 \rangle [1 \pm 0.6 (0.5)]$ , which corresponds to 2.4 dB crest-to-trough ratio. This level of modulation, possibly indicative of the transverse waves behind a large, high-speed (25 knot), range-traveling ship would be difficult

## SAR IMAGE MODULATION

For the low to moderate surface wave conditions in the JOWIP test areas, the linear theory summarized by Alpers et al., (1981) is the only comprehensive theory available for describing SAR ocean wave image modulation mechanisms. This theory is based on a two-scale model of the ocean surface (Wright, 1968). Using this approach, longer gravity waves modulate the microwave backscatter due solely to local wind-generated surface roughness which is assumed to be nearly isotropic and can be described in terms of a saturated wave number spectrum (Phillips, 1977). This roughness is attributed specifically to those short gravity waves traveling radially with respect to the radar and obeying the Bragg resonance condition  $K = 2K_R \sin \theta$ ; where  $K$  is the ocean wave number,  $K_R$  is the radar wave number, and  $\theta$  is the local incidence angle.

The arousal time for SEASAT Bragg resonant waves ( $\sim 30$  cm @  $23^\circ$ ) is estimated to be quite short: approximately 25 seconds for an energy increased by a factor of 3 for a 5 m/s wind. If the wind speed is referenced to 10 meters above the surface and dissipative forces are ignored (Vesecky and Stewart, 1982), this time varies inversely with the square of wind speed between 2 and 20 m/s.

Dissipation of these 30-cm waves is poorly understood and depends on wave-wave interactions, viscous damping, and breaking to sustain wave number saturation of the power spectrum under conditions of increased wind energy input. In the absence of wind input and wave-wave interaction, the clean water viscous energy density decay time (e-folding) for SEASAT resonant (30 cm) waves has been roughly estimated as 450 seconds. In the real ocean this will vary widely and could be an order of magnitude shorter with the introduction of surface films (Phillips, 1977) or strongly interactive waves.

Although alternative formulations for time variant SAR scenes are possible (Hager, 1980; Shuchman and Zalenka, 1978; and Shuchman, 1981), the specific long ocean wave image modulation mechanisms supported by general consensus in the radio-oceanographic community (Vesecky and Stewart, 1982) are:

- tilt of the scattering surface (Valenzuela, 1978);
- hydrodynamically induced crest-to-trough variations in the density of present scatterers (Keller and Wright, 1975); and
- apparent crest and trough coordinate distortions (velocity bunching) caused by long wave orbital velocities (Alpers et al., 1981).

The latter mechanism can result in contrast enhancement for long wave trains but could also smear out the relatively lonesome wave components of a ship wake (Alpers, 1983).

The normalized radar cross-section ( $\sigma$ ) modulation by long ocean waves is statistically described as

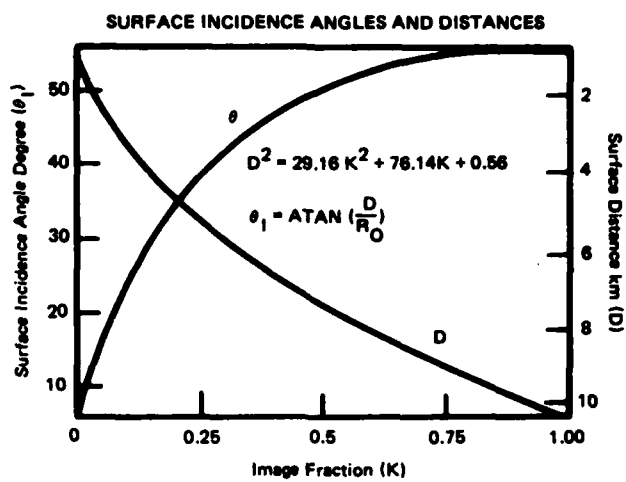


**Figure 5.** Ground incidence angle ( $\theta_I$ ) and ground range (D) as a function of fractional distance (K) from near edge on slant images.

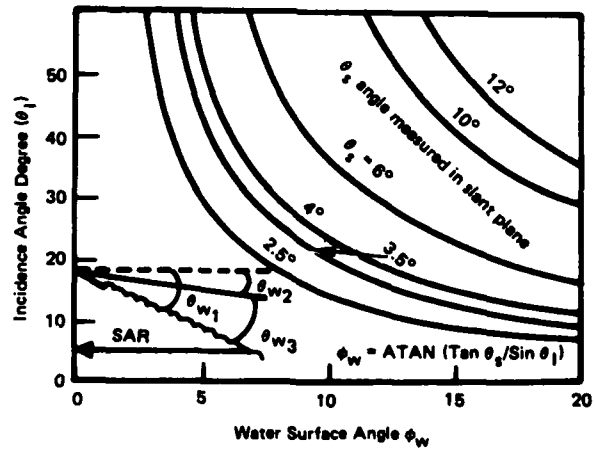


**Figure 6.** Slant-to-ground angle conversion for JOWIP images as a function of surface incidence angle ( $\theta_I$ ).

The imaging geometry for the CCRS/ERIM airborne system is shown in figure 4. Since the primary radar coordinates are range and azimuth angle, all processing is referred to the slant or range azimuth plane as shown in figure 4 where the range delay and 5.4-km sweep translate into a distorted coverage over approximately 10 km on the ground. At the 3-degree nominal incidence used for comparisons with SEASAT, the range distances are considerably foreshortened ( $K \approx 0.1$ ). These foreshortened distances yield small slant plane angles (3 degrees vs 8 degrees) which must be corrected to the ground plane for comparison with the familiar SEASAT surface plane (4-look) nominal 25 meter x 25 meter resolution images. Since all but one of the JOWIP images presented here will be slant-plane, figures 5 and 6 are included to facilitate comparisons.

Figure 5 relates the fractional distances ( $K$ ) (from the near edge of the image to the target area) to nominal local incidence angle ( $\theta_I$ ) and ground distance from nadir ( $D$ ). Figure 6 can be used for conversion of slant to ground angles.

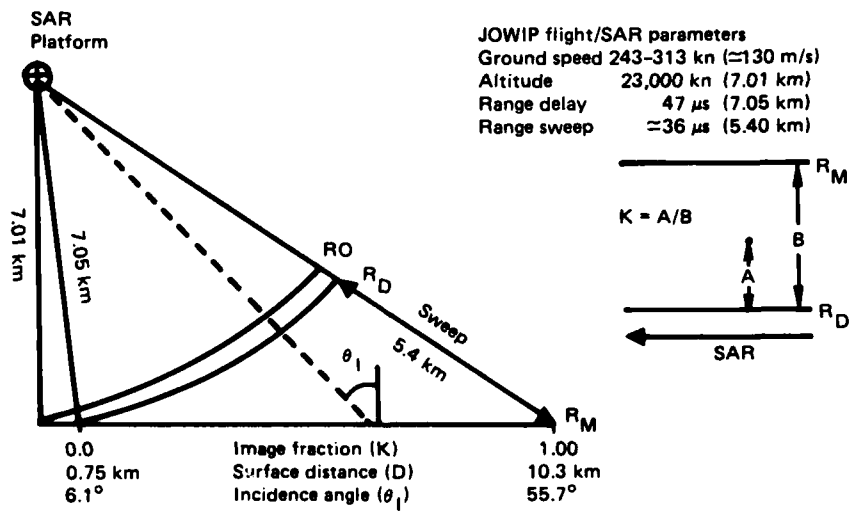


Figure 4. JOWIP surface incidence angles and distances.

Both the phase velocity and  $N(z)$  increase as the density gradient  $d\rho/dz$  increases. In the case of the QUAPAW, intended ship speeds were on the order of 14 knots (7 m/s) which is much greater than possible phase velocities associated with wavelengths near the ship length of 60 m. Here ship speed is above the phase velocity and a narrow vee pattern would be produced behind the ship. The smaller the phase velocity (lower density gradient), the smaller the angle produced in the vee pattern.

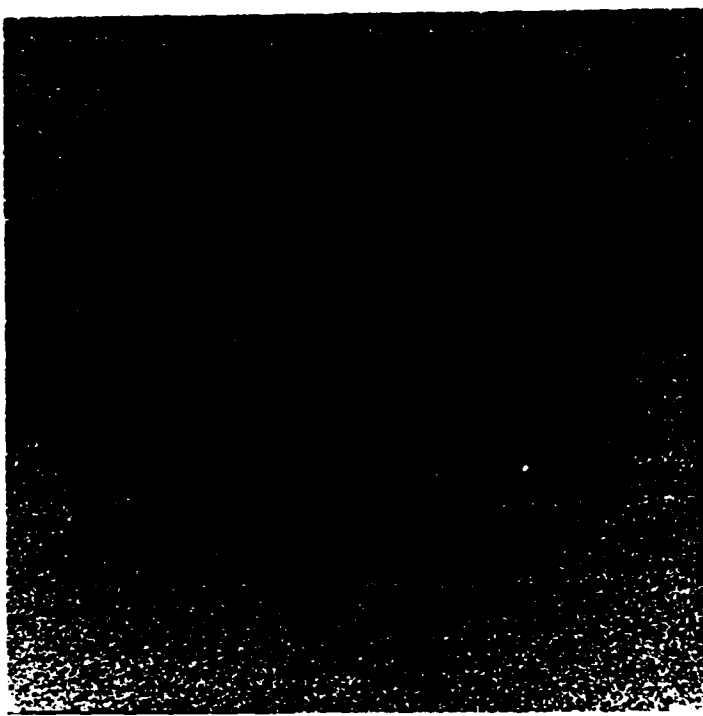
When the turbulent wake is formed, the existing density gradient is temporarily mixed. The density of wake water near the top of the wake is greater than that outside the wake and the reverse is correspondingly true at the bottom of the wake. As this water returns to equilibrium, internal waves are radiated. A vee pattern is again produced by waves traveling away from the ship's speed. The amplitude of these waves depends on the magnitude of the density gradient across the wake and the final height of the wake before collapse. For expected Dabob Bay density gradients the vee angle pattern for QUAPAW was predicted to be 1 degree or less with vanishingly small amplitude.

#### SAR PARAMETERS AND IMAGE FORMAT

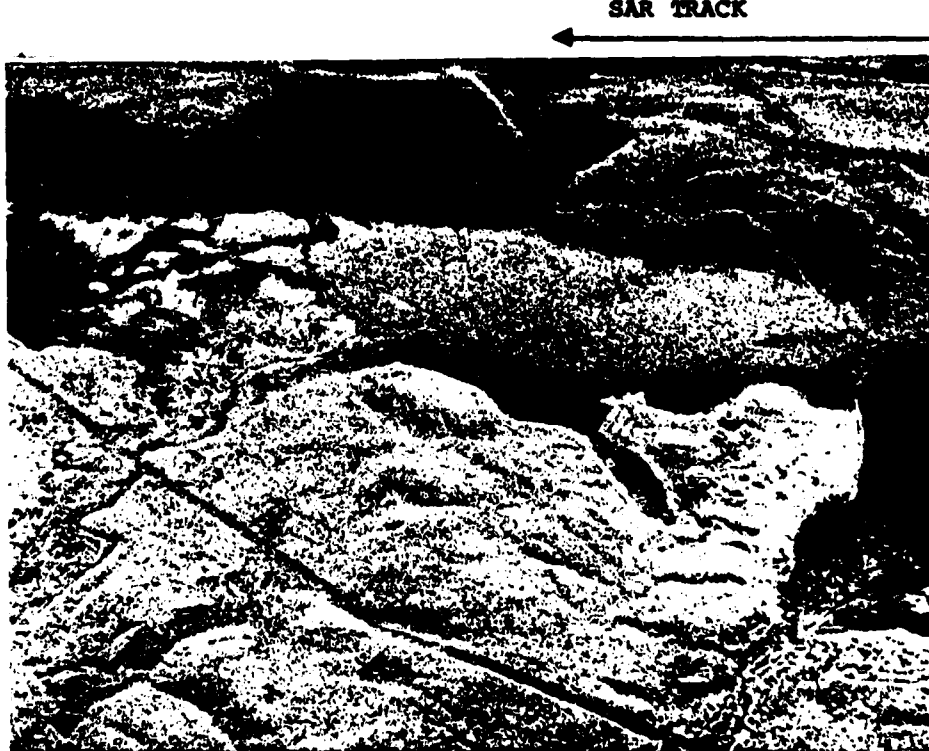
Since the primary objective of the ship wake investigation was to explain SEASAT images it was necessary to adhere as closely as possible to the SEASAT imaging geometry. This involved many tradeoffs including consideration of aircraft capabilities, surface radar incidence, small signal suppression, and emphasis on the horizontally polarized L-band. The primary flight and radar parameters for the SEASAT and CCRS SAR ship wake images were selected by NOSC and ERIM and are shown in table 3 for comparison purposes.

Table 3. Comparative SAR image parameters.

<u>PARAMETER</u>	<u>SEASAT</u>	<u>CCRS SAR</u>
SAR wavelength (L-band) (m) $\lambda_0$	0.235	0.235
Ground velocity (km/s) $V$	7.2	0.13
Altitude (km) $H$	782	7.01
Surface incidence (deg) $\phi$ (ship wakes usually generated at nominal SEASAT 23° incidence)	19 - 25	6 - 55
Mean slant range $R = H/\cos 23$ (km)	850	7.6
Azimuth beamwidth (deg) $\beta_a$	1	6
Bandwidth (MHz) $B_r$	19	60
Ground beamwidth (km) $L = R\beta_a$	89.0 (14 used)	0.796
Azimuth resolution (m) (1-look) $\rho_a = \lambda_0 R/(2TV)$	6.9	5.0
Range resolution (m) $\rho_r = C/(2B_r)$	7.9	3.0
Coherent integration time (s) $T = \lambda_0 R/(2\rho_a V)$	2.0	1.4



A. SEASAT SAR Rev 1404-3, 30 Oct 1978, 04:57:15 GMT



B. JOWIP SAR Flight 9, Pass 1, 28 July 1983, 13:17:08 PDT

Figure 12. Range-traveling ship wake comparison.

estimated by densitometer scans across the SAR image to be 10 dB above the local background (which is estimated at 3 dB above system noise). Also note that the wake shows periodic modulation which closely approximates (40 m) the transverse wavelength associated with ship speed (15 knots). Close inspection reveals that the port and starboard modulations are out of phase revealing a measurable relative azimuth displacement.

Figure 11 shows similar but smaller, narrow-vee, full angles of 5.0 and 3.6 degrees for the SEASAT (23° incidence) and JOWIP (50° incidence) SARs, respectively. These ship headings make an angle of nominally 30 degrees with the SAR ground track. Note that the 50-degree incidence for the bottom image makes specular scattering extremely unlikely as well as indicating less directionality for the ship-induced roughness. While the lower wake image shows a measured modulation length of 35 meters (which could correspond to the transverse waves associated with a 14-knot ship), the upper SEASAT wake image modulation length is a long 140 meters. This case matches more closely the local swell wavelength measured in the wind-roughened area in the upper left and propagating at  $\alpha \approx 135$  degrees relative to the SAR ground track.

For the range-traveling ship comparisons shown in figure 12, the wake arms are completely absent and the only remaining wake characteristic is the turbulent wake aft of the ship. For the top SEASAT image this appears as the usual dark (lack of return) against a wind-roughened background. In the lower JOWIP image, the turbulent wake appears as a bright uniform return across an approximately constant-width turbulent wake viewed against the dark background for this calm wind ( $\sim 0.5$  m/s) case. The sharp returns defining the usual wake arms are absent with reduced image density  $\sim 5$  dB above background. Close inspection of this wake failed to reveal a definite wake modulation length in the bright ship-roughened area. Table 8 summarizes the JOWIP ship wake measurements by date, flight, and pass number. The ship headings ( $|H_o| < 180^\circ$ ) are measured from the SAR track to the ship track and labeled negative (-) if closing and positive (+) if opening range. Angles are positive counterclockwise for the right-looking antenna and positive clockwise for the left-looking antenna. The not resolvable (NR) wake characteristics will all be roughly explained in terms of ambient wind and ship heading.

All the SAR passes except 1-4, 7-1, 7-3, and 9-1 were intended for azimuth-traveling ship wakes. Run 1-4 resulted from an unknown volunteer ship and the latter passes were intended to image range-traveling ship wakes.

In only one case in a localized transitional wind-roughened area during relatively calm conditions (averaged 2.5 m/s) did the L-band SAR produce a recognizable Kelvin wake pattern. This pattern is shown in figure 13 where it is compared with the only known SEASAT image displaying the transverse wave pattern within the Kelvin wake envelope angle.

The SEASAT image, processed by the Royal Air Establishment, to 21 by 12 meter range and azimuth resolution, displays a 94-meter, approximately range-traveling ( $\theta = 104^\circ$ ), transverse wavelength which compares favorably with the measured azimuth displacement ( $\Delta x = 570$  m) for a 23-knot ship:  $V = \Delta x V / (R \sin \theta \sin \phi)$ . Even with the vast ocean surface coverage attained by the SEASAT SAR, high speed targets such as this, moving in the range direction to

Table 8. SAR image measurement summary.  
(lengths and angles corrected to water surface)

SAR Date 1983	Flight-Pass Number	QUAPAN Image Time (PDT)	Relative Ship Heading (deg)	SAR Surface Incidence (deg)	Transverse Wake Comp. Wave length (m)	Turbulent Wake Length (km)	Inner Wake Arm(s) Length Port/Stbd (km)	Angles Port/Stbd (deg)	Kelvin Envelope angle(s) Port/Stbd (deg)
7/23	1-4R	01:53:56	-35 (35)	49.8	35	NR	1.9/2.2	2.0/2.0 <sup>B</sup>	NR
7/26	5-3R	10:17:51	-6 (6)	18.8	NR	2.5 <sup>E</sup>	NR	-	NR
5-4R	11:01:44	172 (8)	20.7	NR	1.1	NR	-	-	NR
7/27	6-1L	15:14:32	-2 (2)	29.6	NR	0.8	NR	-	NR
6-4L	16:14:55	NR (0)	34.2	NR	NR	NR	-	-	NR
7-1L	16:18:34	NR (90)	40.0	NR	NR	NR	-	-	NR
7-3L	17:14:49	NR (90)	32.2	NR	NR	NR	-	-	NR
7-5L	18:26:41	171 (9)	31.0	NR	2.0	NR	-	-	NR
7-7L	19:36:40	175 (5)	24.4	NR	0.6	NR	-	-	NR
7/28	8-1L	07:30:44	167 (13)	29.1	24	2.9 <sup>E</sup>	1.5/1.0	4.0/3.1	NR
8-2L	08:16:09	162 (18)	23.4	40	2.7	1.8/1.7 <sup>E</sup>	3.6/3.6	NR	
8-3L	09:01:18	166 (14)	23.3	40	NR	2.5 <sup>E</sup> /2.4 <sup>E</sup>	2.9/2.9 <sup>B</sup>	NR	
8-4L	09:47:04	161 (19)	41.0	39	2.5 <sup>E</sup>	1.8/0.6	4.4/3.0	16.0/19.4	NR
9-1L	13:16:13	-76 (76)	25.4	NR	1.9	NR	-	-	NR
9-2L	14:00:48	-172 (8)	22.3	38	NR	3.3/3.3	3.0/3.0 <sup>B</sup>	NR	
9-3L	14:46:22	169 (11)	26.6	40	2.4	1.6/1.6	3.0/2.9	NR	

A - Measured 1 km aft unless otherwise stated

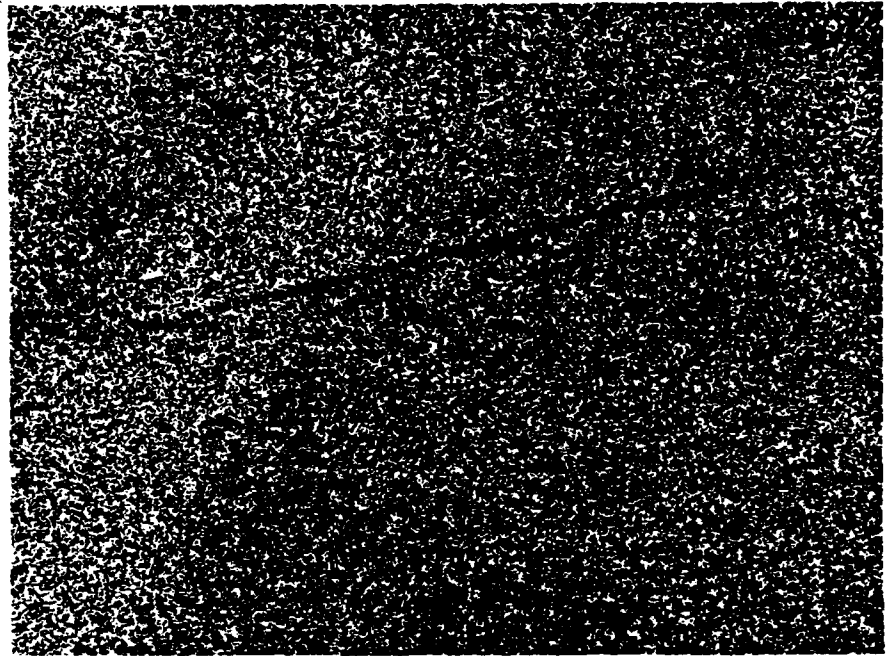
B - Half angles estimated as half the wake angle

E - Length limited by background or path length

NR - Not resolvable

R - Right antenna

L - Left antenna



A. SEASAT SAR Rev 834, 24 Aug 1978, 07:27:12 GMT  
(Courtesy of RAE Farnborough, England)



B. JOWIP SAR Flight 8, Pass 4, 28 July 1983, 09:47:07 PDT

Figure 13. SEASAT and JOWIP transverse wave pattern comparison.

minimize wave motion smear effects (Alpers et al., 1981), are a rare commodity. The average wind speed for this image is unknown.

The CCRS/ERIM image on the lower half of figure 13 also displays the transverse wave pattern with wake half angles ( $\sim 19^\circ$ ) nearer the theoretical Kelvin envelope. However this image is for an azimuth-traveling ship passing through slightly wind-roughened water with a surface radar incidence angle of approximately 41 degrees, a relative ship heading of 19 degrees, and a measured transverse wavelength of 39 meters. Here the entire transverse wave pattern, slightly limited in spots by insufficient surface roughness, is visible.

## DATA ANALYSIS AND DISCUSSION

This section covers special analysis efforts of SAR image data, oblique photography, vertical photography, stereo mensuration, inner wake slope observations, and an analysis summary.

### SAR IMAGE DATA

Reordering the SAR wake measurements presented in table 8 by the local wind speeds shown in table 6 gives us table 9 which clearly shows the effects of local wind speed on JOWIP SAR wake component visibility.

Here wind speeds have been grouped into three categories according to wake component visibility. For the first essentially flat calm category, the dark (lack of return) turbulent wake is not seen. On run 9-1 the turbulent wake is clearly due to the increased scatter generated by the range-traveling ship as are the arms apparent for the azimuth-traveling ship on run 9-2.

For the transitional wind category, the situation is somewhat more complex with turbulent wake measurement complicated by the ship passing in and out of small local wind-roughened patches. The important observation here is that under these wind conditions the ship-generated surface roughness persists in the locally calm areas along the track and gives rise to measurable narrow wake angles. These narrow angles are further seen to exist for relative ship heading out to at least 35 degrees and for radar surface incidence angles between 23 and 50 degrees. In only one case (run 8-4) at the upper end of this wind category, was a wind-generated surface roughness of 2.5 m/s barely adequate to reveal the full width of the transverse pattern between the Kelvin wake envelope arms. The wind speed of 3.5 m/s is the estimated speed required to maintain a saturated spectrum of first order Bragg scattering (30 cm) gravity wave roughness (Vesecky and Stewart, 1982).

The transverse ship wake waves in the wind-roughened category were probably not of sufficient amplitude ( $< 0.5$  m) to be visible by the usual image modulation mechanisms (Vesecky et al., 1982). The last trace of the wake, the turbulent patch, disappears at the higher wind speeds ( $> 10$  m/s) making even the SAR determination of ship heading impossible.

### SAR WAKE IMAGE MODULATION LEVELS

In order to quantify the observed image modulation levels, a series of cross wake (radar range direction) scans were run on an ERIM optical processor. For this evaluation a calm surface portion of the wake on SAR run 8-2 between 800 and 1200 meters aft of QUAPAW was selected. The scans were accomplished in the slant range plane using an 8-meter-diameter aperture; each line scan was plotted as linear intensity versus slant range to explore the effects of observed transverse wave ( $\lambda = 40$  m) modulation over a 10-wavelength interval (51 scan lines). Figure 14 shows an example of five of the 51 consecutive scans across the wake with an approximately 8-meter along-track spacing between scans. The side-to-side asymmetry is apparent as are multiple smaller peaks in addition to the predominant ones responsible for narrow wake arms.

Table 9. Wind influence on SAR observable ship wake structures.

SAR Run Pit-Pass	Wind Speed (m/s)	Relative Ship Heading (°R)	Transverse Wavelength (cal/crosses) (m)	Radar Incidence Angle (deg)	Inner Wake Arm(s) (P/S) (km)	Kelvin Envelope (P/S) (deg)	Turbulent Wake Length (km)
<u>Locally calm winds (&lt;1 m/s)</u>							
9-2	<1	8	42/38	22	3.3/3.3	3.0/3.0 <sup>B</sup>	NR
9-1	<1	76 RG	40/NR	25	NR	NR	1.9 <sup>E</sup>
<u>Transitional Winds (1 to 3.5 m/s)</u>							
1-4	-	35 (OB)	-/35	50	1.9/2.2	2.0/2.0 <sup>B</sup>	NR
8-2	1.5	18	41/40	23	1.8 <sup>E</sup> /1.7 <sup>E</sup>	3.6/3.6	NR
9-3	<2	11	41/40	27	1.6/1.6	3.0/3.9	NR
8-1	2.2	13	26/24	29	1.5/1.0	4.0/3.0	NR
8-3	2.5	14	40/40	23	2.5 <sup>E</sup> /2.4 <sup>E</sup>	2.9/2.9 <sup>B</sup>	NR
8-4	2.5	19	41/39	41	1.8/0.6	4.4/3.0	18/19.4 <sup>E</sup>
<u>Wind-Roughened Surfaces (&gt;3.5 m/s)</u>							
5-3	5.1	6	28/NR	19	NR	-	NR
6-1	6.0	2	-27/NR	30	NR	-	NR
6-4	6.4	AZ	27/NR	34	NR	-	NR
7-7	6.5	5	-27/NR	24	NR	-	NR
7-5	7.0	9	-27/NR	31	NR	-	NR
5-4	7.7	8	-27/NR	21	NR	-	NR
7-3	9.7	RG	-27/NR	32	NR	-	NR
7-1	11.2	RG	-27/NR	41	NR	-	NR

Note: All angles and lengths corrected to the ground plane

RG - approx range-traveling ship

AZ - approx azimuth-traveling ship

OB - roughly diagonal or oblique-traveling ship

NR - not resolvable

E - length limited by roughness background variation and/or distance traveled

B - angles shown are half full angles necessitated by absence of turbulent wake

R - positive radar return against dark background

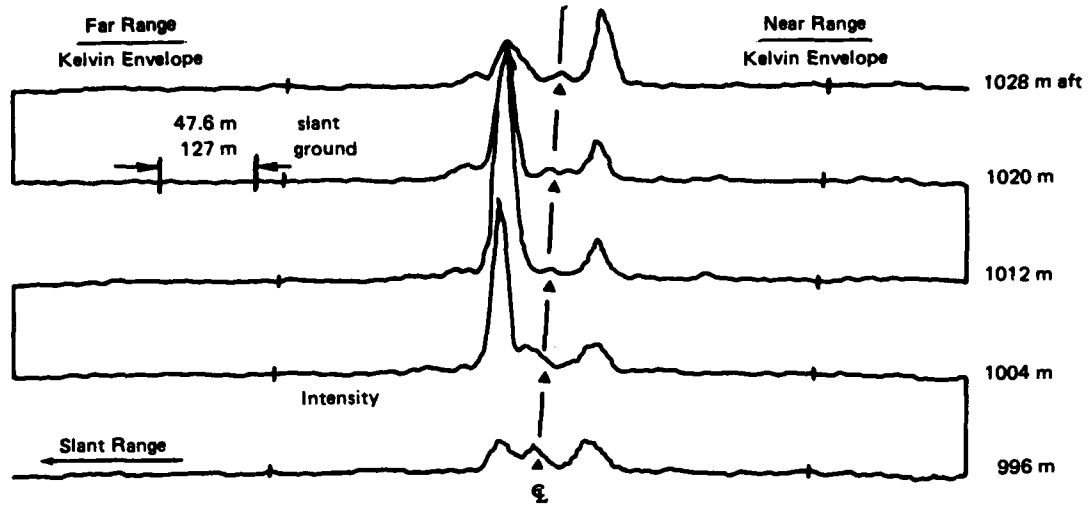


Figure 14. Linear intensity versus radar range across QUAPAW wake (Run 8-2); ERIM optical processor, 26 March 1984.

Statistics for the entire 51-scan data set are shown schematically in figure 15. In treating these data the wake centerline was determined for each scan line by bisecting the distance between the major peaks. The distances of each of the peaks from this centerline were then measured and they consistently fit into reasonably well defined groupings centered about the wake coordinate angles shown with the frequencies indicated. The amplitudes were then measured for the background and each peak along with these linear intensity values converted to the mean decible values shown in the figure. Note that a peak (AV 6.4 dB) occurred between the major peaks in 57 percent of the cases and that in the remaining 43 percent of the scans the centerline image intensity was 3.7 dB above this locally calm background level. We suggest that a wind-induced 7-dB increase in the background level would eliminate all but the major peaks and result in the usual dark (lack of return) turbulent wake along the ship's track. Of possible significance are the very low frequency and amplitude associated with the Kelvin wake envelope and the generally higher amplitudes on the far range side of the wake.

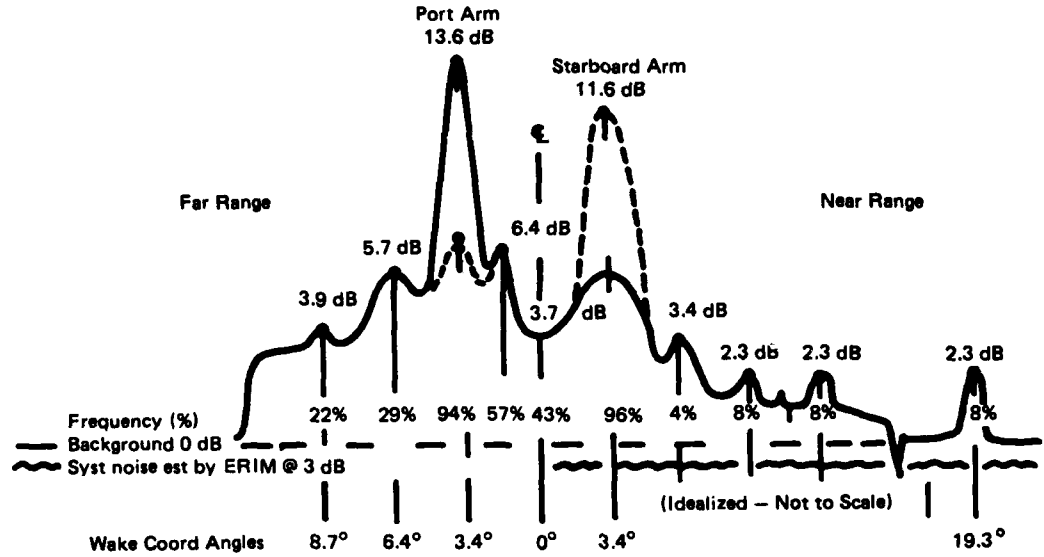


Figure 15. SAR wake image scan statistics for calm water (SAR pass 8-2).

Along-track spacing of peaks was estimated from along-ship track wake-arm fluctuations in image intensity to be  $(43 \text{ port} + 46 \text{ starboard})/2 = 44.5$  meters. Attempts to quantify the side-to-side phase difference have been less successful but something close to half the transverse wavelength appears probable from inspection of images. If the ship-induced roughness is associated with short gravity waves propagating in roughly opposite cross-track directions, then a phenomenon analogous to doppler-splitting (Alpers et al., 1981) might cause a nominal 15-meter azimuth offset of the amplitude peaks.

It must be pointed out that the along-track wake arm modulations varied between 7 and 16 dB on the far range side of the wake and between 6 and 14 dB on the near range side. These peak-to-trough differences of 9 and 8 dB are far in excess of the theoretical predictions for tilt or hydrodynamic image modulation but very close to the velocity-bunching modulation level (7 dB) predicted in table 4. We therefore conclude that an effect like "velocity bunching," as described by Alpers (1979, 1981, 1983), caused by transverse wave orbital motion, is the SAR image modulation mechanism responsible for narrow wake images.

#### OBLIQUE PHOTOGRAPHIC OBSERVATIONS OF SURFACE ROUGHNESS

Figures 16 and 17 illustrate the effects of low wind speed surface roughness on a SAR image. The SAR image in figure 16A covers a 7.4-kilometer,

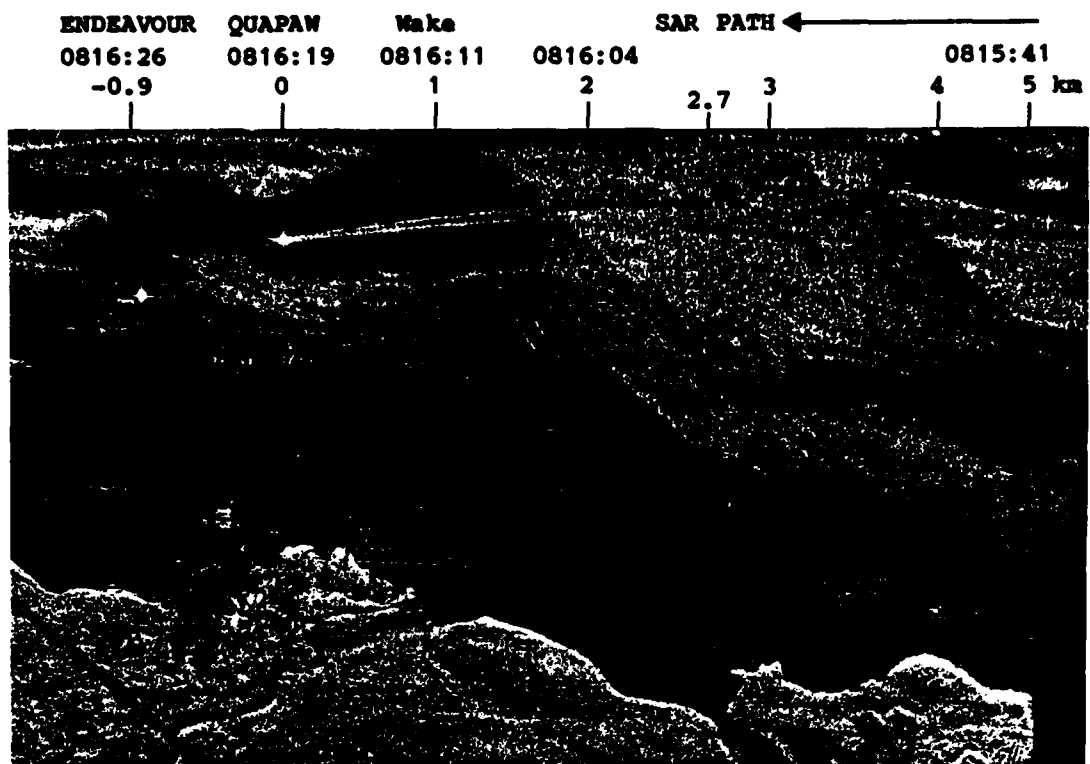


**Figure 16A.** Surface roughness variation along SAR run 8-2.  
Azimuth Scale: 7.7 s/km.

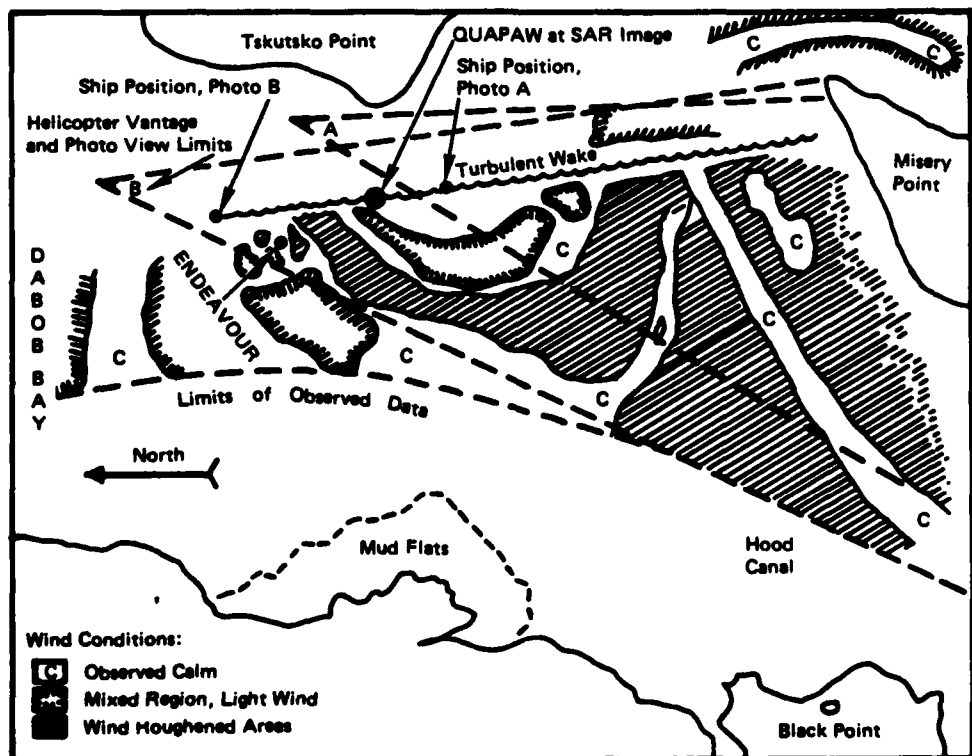


**Figure 16B.** Surface roughness variation from photographic compilation.

Turbulent Wake



Figure 17A. Photo of turbulent wake flattening and sharp edge between rough and smooth areas. DREP PHOTO: 728081507



Figure 17B. Photo of surface roughness in the vicinity of CFAV ENDEAVOR. DREP PHOTO: 728081848

left-looking slant range segment of run 8-2. The image times were approximately 0815:30 to 0816:30 PDT and the average wind speed recorded aboard ENDEAVOUR (shown in figures 16A, 16B, and 17B) over the interval 0812-0817 was  $1.5 \pm 0.3$  m/s, temporal average. The SAR image suggests a considerable spatial variation in surface roughness and the intent of this example was to correlate qualitative estimates of surface roughness from photographic coverage with the SAR image.

Six aerial photos were shot from 1000 feet, over an interval of 5.5 minutes spaced around the 1-minute necessary for the SAR image. Figure 16B shows a composite of subjective surface estimates on a partial chart of Dabob Bay. The wind-roughened areas were estimated from six oblique aerial photos; the two most helpful are shown as parts A and B of figure 17. Figure 17 shows the scar caused by passage of the QUAPAW through a locally wind-roughened area looking southeast 1-minute before SAR time. Notice how the turbulent wake has calmed the wind-roughened area in the upper left corner; notice also the sharp edge between the smooth and roughed-up areas. This transition between roughened and calm areas is remarkably abrupt and these abrupt lines strongly persist from photo to photo over many minutes of elapsed time, resulting in a quasi-standing rather than a propagating surface wave disturbance. The sharp edges of these patterns are easily seen on the SAR image as it slants off to the upper left corner. Figure 17B was imaged over 2 minutes after the SAR pass, and shows water surface detail near the Canadian ship ENDEAVOUR as it moves slowly across the QUAPAW's wake at a heading of 090°T. Notice how the composite diagram of roughened surface areas from the oblique photos closely matches the SAR image pattern of the same scene. Notice also that since the turbulent wake strip produces a lack of return on the SAR image, it is not visible in the calm area between two narrow-angle arms of the wake, but is only evident when there is a sufficiently roughened surface to show this lack of radar return. These roughened background areas are thought to be populated by capillary and short gravity waves with centimeters amplitudes.

#### VERTICAL PHOTOGRAPHY FOR SHORT GRAVITY WAVELENGTH AND HEIGHT DETERMINATION

Vertical photographs taken over the Dabob Bay SAR events fall into two altitude regimes. We took a sequence of color runs covering the entire wake system in a series of single frames (135 m x 135 m) taken from a 750-foot altitude, only during DREP run 9-1. The bulk of the photography, however, was high resolution black and white stereo pairs covering small sectors (60 m x 60 m) of the wake system taken from a 200-foot altitude. All frames are nominally 2 x 2 inch format (70 mm film). Using both these photo sources as single frames for wavelength extraction will be discussed here and a brief description of progress on stereo analysis of instantaneous ocean surface topography will follow in the next section.

One of the color photo runs, a short sequence of frames on both the port and starboard sides of the wake pattern approximately 1000 meters aft of the ship was used for preliminary estimate of wake wavelengths and propagation directions with respect to the ship's track. These parameters are plotted in figure 18 where they are compared with the calculated Kelvin wake parameters defined by equations (2) and (3). Wake wavelengths about 10 meters on this calm wind interval compare favorably with the calculated Kelvin wake values,

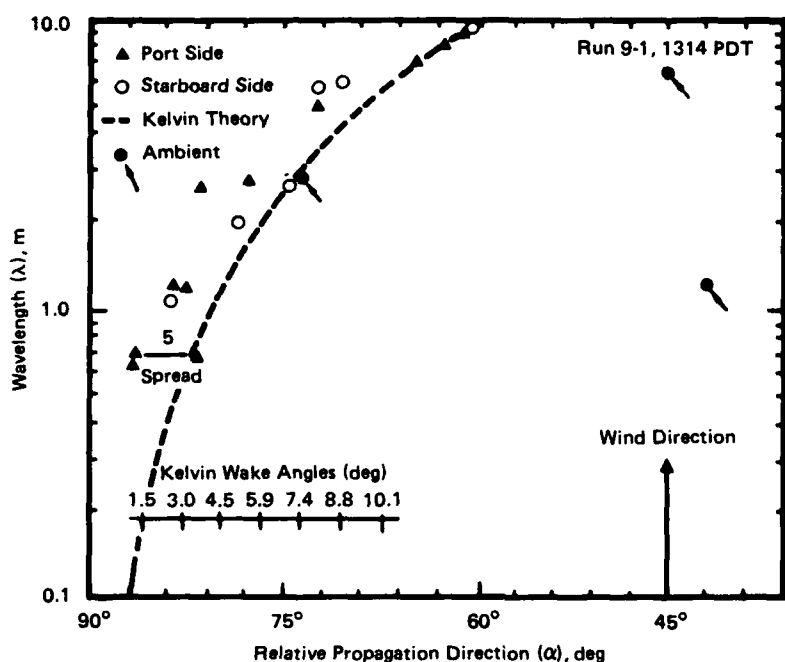


Figure 18. Preliminary photographic estimates of ship wake component wavelength vs relative propagation angle (run 9-1).

but below 10 meters all measurable wavelengths were equal to or greater than the calculated Kelvin theory predictions.

Also included in figure 18 are several ambient wave components which compare favorably with the average wind direction, also indicated in the figure. This may be fortuitous at these low wind speeds (< 1 m/s) where wind direction commonly wanders.

The observed surface wavelength deviations from the Kelvin theory could result from (1) background wave clutter; (2) inappropriate directional sun-sky illumination at various phases (slopes along the longer transverse wavelengths); (3) reduced slopes, and therefore reflected light from these shorter wavelengths; or (4) failure of simple Kelvin model predictions at these short wavelengths.

It must be emphasized that, while photographically observed wavelengths and propagation directions are valid, the same wavelength propagating in another direction might not be as obvious. Further, we cannot state that because shorter wavelengths are not apparent on the photos, they are not present in the scene.

Since items (1) and (2) above were under reasonable control by site selection, ship track orientation, and luck, items (3) and (4) (which must also be considered for all the photographic records) were felt to be the critical factors. Approximate sun azimuth and elevation for each QUAPAW wake run are given in table 10. For vertical photography, the table also gives the critical slope angles required for direct sun glint or glitter, equal to half the sun's zenith angle. Problems associated with using the width of the glitter patterns, which vary with surface slope (Hulbert, 1934) and with the statistical extraction of two-dimensional slope spectra from within glint pattern photographs (Cox and Munk, 1954), were to be avoided here by using a method analogous to the optical transform method of Stillwell (1969). By working outside the glitter pattern and relying on a continuous skylight luminance, we hoped that surface measurements could be made with a minimum of directional, slope, and wavelength bias.

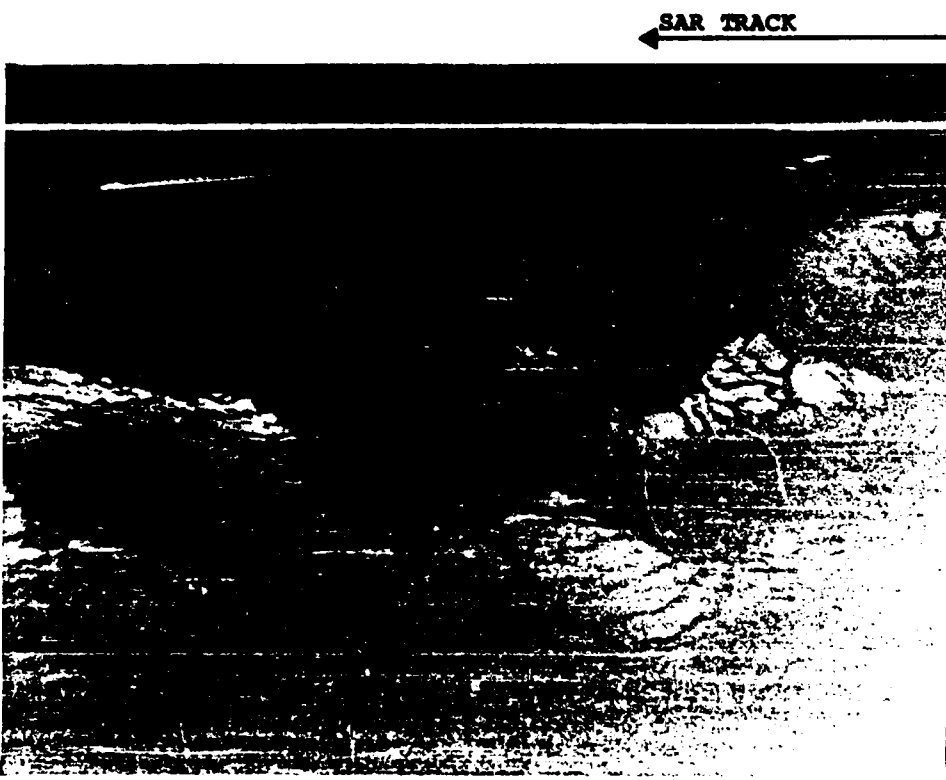
Table 10. Sun azimuth and elevation for photographic ship wake runs (47-41N; 122-15W).

Run	Time (PDT)	Sun Azimuth (deg)	Sun Elevation (deg)	Critical Angle (deg)
7-1	16:18:54	247	46	22
8-1	07:30:44	79	16	37
8-2	08:16:09	88	24	33
8-3	09:01:18	96	31	30
8-4	09:47:04	105	39	26
9-1	13:16:13	178	61	15
9-2	14:00:48	200	60	15
9-3	14:46:22	218	56	17

Using the sequence of vertical photos from the low altitude run (8-3) positioned in wake coordinates in figure 19, the subdivided (10 m x 10 m) regions between grid marks were digitized using a 50-micron aperture scanning densitometer on the 70-mm original negatives. From this process digital two-dimensional fast Fourier transforms (FFT) of the 192 x 192 square array were obtained. The associated FFT numbers are also shown in the figure along with a typical frame (#13). The entire run, frames 1-23 covered the path shown from 900 meters aft to over 300 meters ahead of the ship. Because the wake center-line was visible and the ship travel speed and aircraft flight parameters known, this photo track was established at a 10-degree crossing angle. Adjusting this flight line from ground coordinates to the stationary ship wake coordinate system changes this crossing angle to the 13 degrees shown on the drawing. The wake angles and distance aft of the ship corresponding to each FFT are included in the data tables to follow.



A. L-band ERIM radar



B. X-band ERIM radar

Figure 28. Simultaneous X- and L-band narrow wake images in Georgia Strait, 27 July 1978 (pass 2).

Table 15. Estimated surface wavelengths for JOWIP inner wake arms table 8.

SAR Run	First order Bragg wavelength (cm)	Nearest cross-track (cm)	Other arm
8-1*	24	50+20	31+20
8-2	30	63+30	63+30
8-3	30	41+30	41+30
8-4	18	95+30	44+30
9-2	31	44+30	44+30
9-3	26	44+30	41+30

\*V = 6.5 m/s



Figure 27. ERIM digitally processed JOWIP ship wake image (run 8-2).

should be tested against other extreme parametric variations. Figures 28A and B show a slant range comparison of a narrow wake image made by the same ERIM SAR in 1978 with both X- and L-bands functioning properly. While the L-band shows a much stronger wake with a 4.7-degree (ground range) wake angle, at this steep incidence ( $18^\circ$ ) the X-band also shows a shorter narrow wake at 3.7 degrees (ground range half angle), which is modulated by a 54-meter transverse wavelength (17.8-knot ship). For X-band at this incidence, the Bragg length is approximately 5 cm and the wake extends for 2.5 km.

Table 14. Comparison of wake angles (deg) with Bragg resonant wavelengths (cm) for various incidence angles (deg).

(Azimuth Traveling Ships  $\phi = 0$ )

Radar Incident Angle ( $\theta_i$ )	20	23	25	30	40	50	90
1st order Bragg wavelength ( $\lambda_B$ )	34.4	30.1	27.8	13.5	18.3	15.3	11.8
Kelvin wake angle ( $\theta_K$ )	2.6	2.5	2.4	2.2	1.9	1.7	1.5
Cross-track roughness angle ( $\theta_C$ )	2.7	2.5	2.4	2.2	1.9	1.8	1.6
2nd order Bragg wavelength ( $\lambda_{2B}$ )	68.8	60.2	55.4	47.0	36.6	30.6	23.6
Kelvin wake angle ( $\theta_K$ )	3.7	3.5	3.4	3.1	2.7	2.5	2.2
Cross-track roughness angle ( $\theta_C$ )	3.8	3.5	3.4	3.1	2.7	2.5	2.2

Substituting the deep water gravity wave dispersion relation in equation (13) gives

$$\lambda_c \approx (8\pi V^2/g) \tan^2 \theta_c, \quad (14)$$

so that the change in apparent wavelengths with wake angle and ship speed measurement errors can be written as

$$\Delta \lambda_c \approx \left[ \frac{16\pi V \tan^2 \theta_c}{g} \right] \Delta V + \left[ \frac{16\pi V^2 \tan \theta_c \sec^2 \theta_c}{g} \right] \Delta \theta_c. \quad (15)$$

Using approximate JOWIP parameters ( $V = 8$  m/s,  $\theta = 3^\circ$ ,  $\phi = 0^\circ$ ), we obtain  $\Delta \lambda_c \approx 0.113 \Delta V + 17.251 \Delta \theta$ , which means that the apparent surface wavelength will be in error by approximately 30 cm per degree wake measurement error. The variation with ship speed is much less significant at approximately 5 cm per knot where the average ship speed error is estimated at  $\pm 0.5$  knot.

Converting the measured inner wake angles for azimuth-traveling ships (table 8) into estimated surface wave wavelengths (table 15) by equation (14) indicates gravity wavelengths considerably in excess of first order Bragg resonance, barring as yet undiscovered bias in the SAR angle measurements.

As digitally processed ground-range-corrected images like the example for run 8-2 (figure 27) (Shuchman, 1984) become available, refined wake angle measurements will help provide better SAR estimates of surface wavelengths for comparison with photographic results. The measured wake angle from this image is almost 1 degree narrower than the corrected estimate based on measurements from the slant range image.

During JOWIP, we emphasized the horizontally polarized L-band SAR mode. Use of the X-band JOWIP images was severely restricted by antenna problems which made most of these images almost unusable at the near nadir ( $23^\circ$ ) SEASAT-like incidence, where our primary wake coverage was grouped. It must be pointed out that the X-band ship wake data have been reported elsewhere (Hammond et al., 1983) and that appropriate explanations of wake wave imaging

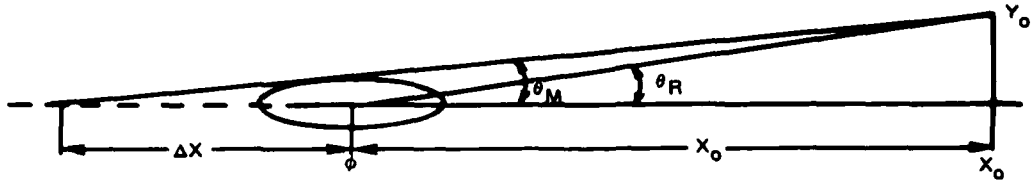


Figure 26. Definition of radar and modeled wake angles.

For ships with significant beam, such as QUAPAW (length 60 m, beam 12 m, draft 4 m), the source of the shorter wavelengths will be assumed to be at the center of the ship so that a revised wake angle  $\theta_w = \text{atan} (Y_o - 6)/X_o$  will be used for measurement purposes. This will reduce the half wake angles of interest in our nominal 1-km aft wake area by  $\sim 0.3$  degree and will result in the  $\Delta X$  values shown in table 13 for the range of QUAPAW wake angles of interest. This later ( $\theta_w$ ) is the angle listed for all photo wake data.

Table 13. SAR versus estimated model wake angles for 1-km aft wake measurements.

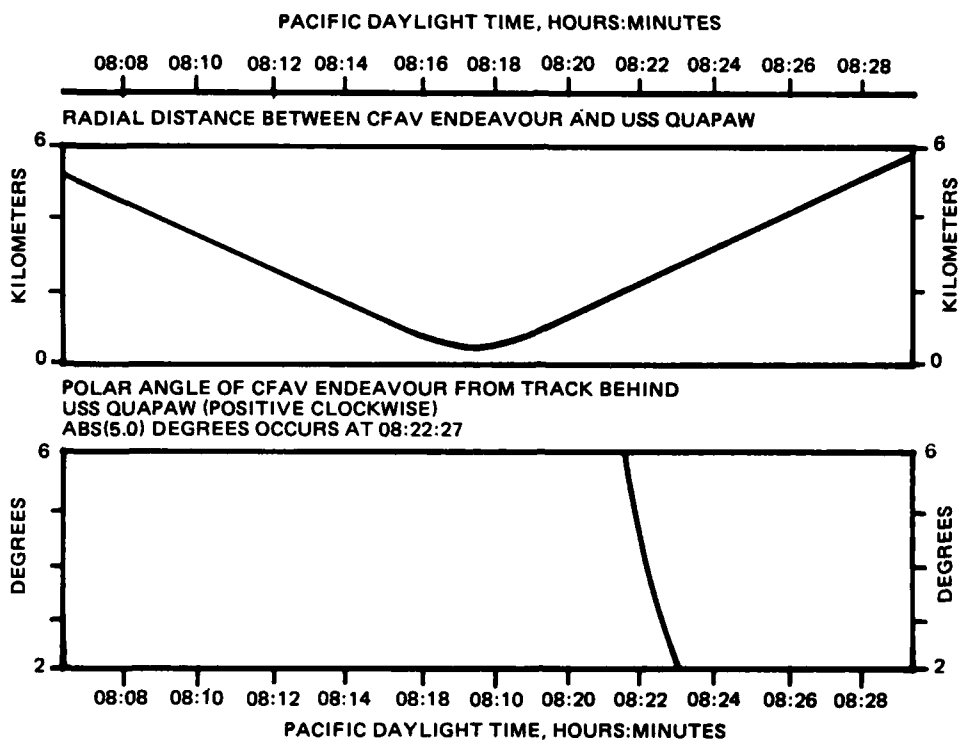
$\theta_R$ (deg)	1.5	2.0	2.5	3.0	3.5	4.0
$\theta_w$ (deg)	1.2	1.7	2.2	2.7	3.2	3.7
$\Delta X$ (m)	299	172	156	127	107	93

Recognizing that the enhanced populations of ship-generated short wavelengths identified in the photographs along the observed wake arms propagate with group velocity  $C_g$ , roughly perpendicular to the ship track, we may write the cross-track roughness radar wake angle ( $\theta_c$ ) as

$$\theta_c \approx \text{atan} \left( \frac{C_g}{V} \right), \quad (13)$$

which for  $\theta$  small and  $\theta \approx 0$  is approximately equal to the more general  $\text{asin}[(C_g/V) \cos(\theta - \phi)]$  suggested by Munk (1984).

A comparison between equation (13) and the Kelvin wake angle for first and second order Bragg resonant wavelengths for various surface radar incidence angles is shown in table 14. The maximum variation of Kelvin wake components from the ship cross-track direction is only 7 degrees and the wake angles differ only by 0.1 degree, which is clearly beyond the precision of the present measurements. Actually we estimate the maximum error in the measurement of surface radar wake angles presented in this report to be approximately  $\pm 1$  degree which means that additional work at higher resolution and as far aft as possible will be required to differentiate between the first and second Bragg resonant angles.



**Figures 24.** CFAV ENDEAVOUR and USS QUAPAW relative positions in Dabob Bay, run 8-2 (courtesy of DREP).

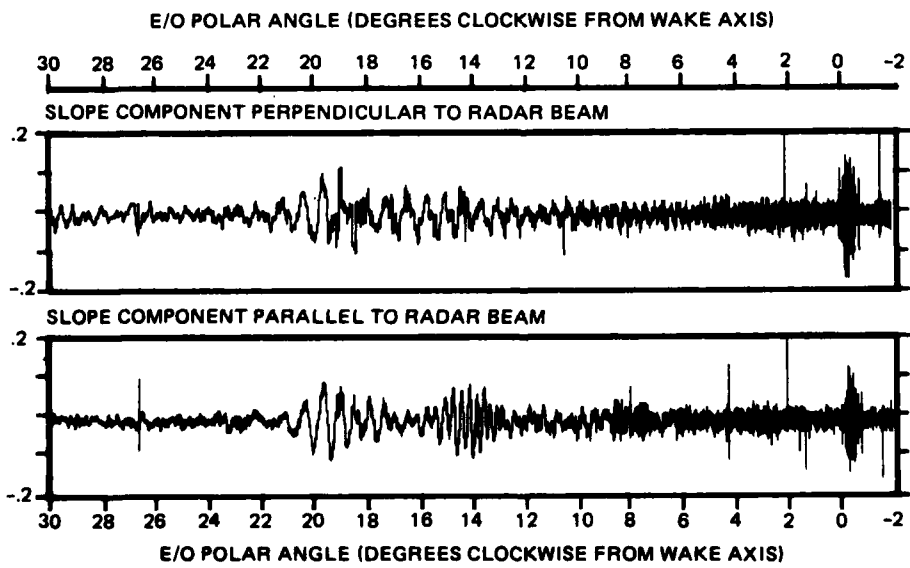


**Figure 25.** Wave slope components perpendicular and parallel to the radar beam (courtesy of DREP).

Taking raw height data from the different contractors for the 40 comparison grid points (shown in figure 22C) allows comparison after the data sets are leveled. Since our desired output is relative height over wavelengths that are short compared to the image size, the initial heights were measured relative to an estimated reference plane which displays an overall tilt caused by aircraft attitude and long wave slope. The data for model 9's reference grid points have been leveled and the remaining mean differences reflect a vertical bias. The mean differences between contractors and between operators shown in figure 23B do not affect relative heights.

Preliminary study of specific grid points shows a single operator repeatable height resolution of  $4.4 \pm 3.5$  cm (figure 22A) for this cloudy day. This primary factor is dependent on surface lighting conditions and altitude, and must be statistically evaluated for each stereo model. No attempt has been made or is planned to bridge the surfaces between stereomodels. It is sufficient to position the model and its small scale roughness with respect to phase on the transverse wake waves, wake angle, and distance aft.

#### INNER WAKE SLOPE OBSERVATIONS

The CFAV ENDEAVOUR carried a two-dimensional laser wave slope instrument which provided high resolution, 400-Hz data on changes in the surface wave slope during passage through a Kelvin wake wave event. When combined with the trisponder positioning data an accurate determination of surface roughness changes within the wake can be made for comparison with the radar image intensity.

Figure 24 shows the relative positions of the ENDEAVOUR and QUAPAW during run 8-2. These data provide the time ENDEAVOUR reached a given wake angle (for example  $3^\circ$  @ 08:22:27) to queue data from the slope sensor. Figure 25 gives an example of DREP's data reduction (Hughes, 1984) combining these data into slope components perpendicular and parallel to the radar plane of incidence as a function of wake angle. These data show small wave slopes ( $< 3^\circ$ ) in the 1-3 degree portion of the wake system and about 6-degree angles on the Kelvin cusp waves. Background wave angles were apparently on the order of 0.5 degrees.

These preliminary data tend to rule out specular scattering but more detailed analysis is required before this can be confirmed.

#### ANALYSIS SUMMARY

An important source of wake angle variation, especially when making measurements close to the ship, is the location of the point selected for the vertex of the wake angle. Kelvin wake angles intersect the ship's track some distance ahead of the ship (Inui, 1962), while most measurements of narrow azimuth, traveling-ship wake angles made on SAR images use the ship itself as the vertex. Thus SAR observed wake angles defined in terms of measured ( $X_R$ ,  $Y_R$ ), as shown in figure 26 ( $\theta_R = \text{atan} [Y_R / X_R]$ ), result in the SAR angle ( $\theta_M$ ) being larger than the theoretical wake angle ( $\theta_K$ ).

**(A) Comparison between contractors stereomodel setup parameters (outer camera orientation)**

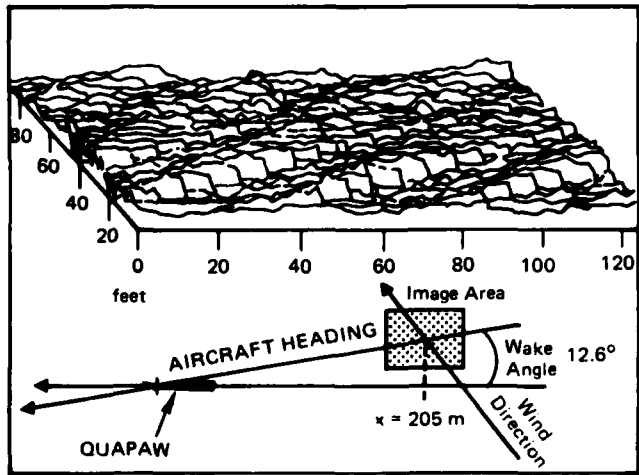
CONTRACTOR	AIRCRAFT		RELATIVE ORIENTATION <sup>3</sup>			
	$\Delta Y$ (ft) <sup>1</sup>	$\Delta Z$ (ft)	TILT <sup>2</sup>	$\Delta\omega$ <sup>4</sup>	$\Delta\phi$ <sup>5</sup>	$\Delta\kappa$ <sup>6</sup>
A	34.996	-0.53	0.87°	0.244°	4.639°	-1.471°
B	35.00	0.00	0.0°	-0.017	4.4421°	-1.348°
C	34.3	-1.31	2.14°	0.153°	4.584°	-1.314°

NOTES: 1.  $\Delta Y$  VALUE GIVES THE CAMERA BASELINE USED IN MODEL SETUP.  
 2. THE TILT IS GIVEN BY  $\tan^{-1}(\Delta Z/\Delta Y)$ .  
 3. FOR CONVENTIONAL IN-LINE STEREO WORK, THE FULL ANGLES MEASURED ARE:  
      $\omega$  - PITCH      $\phi$  - ROLL      $\kappa$  - YAW ANGLE.  
 4. THE  $\Delta\omega$  VALUE IS THE LEAD/TRAIL BETWEEN THE CAMERAS ALONG THE Y-AXIS.  
 5. THE  $\Delta\phi$  VALUE IS THE CONVERGENCE ANGLE BETWEEN CAMERAS (TOE-IN).  
 6. THE  $\Delta\kappa$  VALUE IS THE ROTATION ANGLE ABOUT THE VERTICAL Z-AXIS.

**(B) Comparison of separate measurements (leveled data points) for left and right camera reference grids**

COMPARISON	CAMERA	MEAN DIFFERENCE		STANDARD DEVIATION (cm)
		(cm)	(cm)	
BETWEEN CONTRACTORS (A-B)	LEFT	7.0	5.1	
BETWEEN OPERATORS (C)	RIGHT	7.7	7.4	
BETWEEN LEFT	6.8	6.2		
RIGHT	NO COMPARISON AVAILABLE.			

**(C) Three-Dimensional Plot: taken from spot reading grid of 2562 points, showing image position in wake. (Model 9)**



**(D) Wake profiles near QUAPAW (Model 12)**

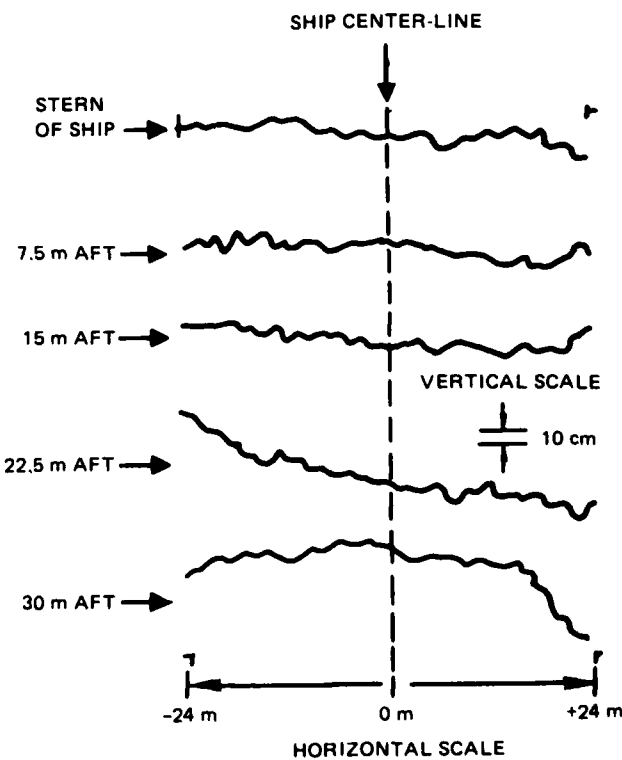
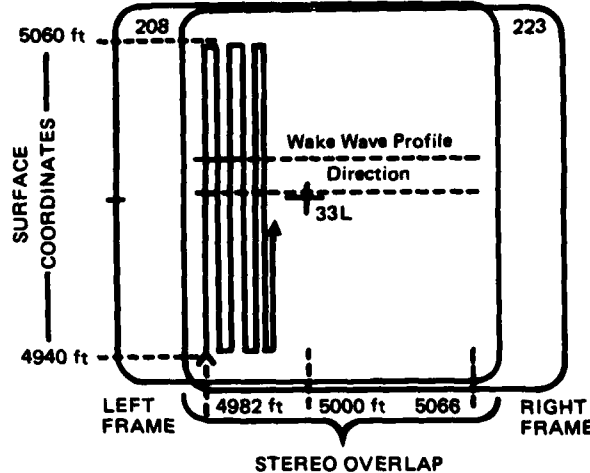


Figure 23. Stereomodel analysis approaches.

(A) STEREOMODEL 9



DATA COLLECTION

Aircraft Altitude: 54 m  
Speed: 61.4 m/sec  
Date: 27 July 1963  
Run: DREP 7 Pass 1  
Time: 1613:31 PDT  
Stereomodel: 89  
Conditions: windy with broken clouds.  
Wind: 11.2 m/s, 200°T

POSITION IN WAKE

Aft of source (bow): 200 m  
Side: 45 m to starboard  
Half wake angle: 12.6°  
(to center of frame)

DATA ANALYSIS SUMMARY

Spot readings: 2562 points  
Grid spacing: 0.6 x 0.6 meter on surface  
Aspect: 42 rows of 61 measurements  
Rotation: none, parallel to side of frame

Statistical Spot Height Resolution

Achieved: 4.4 ± 3.5 centimeters

COMPARISON OF GRID POINTS FOR MODEL 89, DREP 7-1

GRID	Y-VALUE	X-VALUE	Z (A)	Z (B)	Z (C)
------	---------	---------	-------	-------	-------

CAMERA 208

25L	4971.2	5037.4	1.171	1.063	---
35L	5000.1	5058.1	-0.046	0.000	-1.121
45L	5029.4	5058.6	-0.509	-0.188	-0.495
55L	5059.2	5059.1	-0.407	-0.783	0.636
24L	4971.3	5028.6	1.572	2.119	---
34L	5000.0	5028.9	1.005	0.995	0.482
44L	5029.4	5029.3	-0.480	-0.394	-0.484
54L	5059.1	5029.7	-0.881	-1.880	-0.310
23L	4971.3	5000.1	0.951	1.530	---
33L	5000.0	5000.0	0.741	1.103	0.483
43L	5029.3	5000.0	0.174	0.000	0.405
53L	5059.4	5000.0	-0.603	-1.911	-0.364
22L	4971.2	4971.1	0.055	0.588	---
32L	5000.0	4970.9	-0.306	-0.088	-0.073
42L	5029.4	4970.6	-0.198	-0.321	---
52L	5059.0	4970.2	-0.740	-1.646	0.131
21L	4971.3	4942.6	1.132	1.724	---
31L	5000.0	4941.7	-0.118	0.000	0.202
41L	5029.6	4940.9	-0.816	-1.694	0.225
51L	5059.5	4940.5	-0.498	-2.023	0.289

CAMERA 223

15R	4965.5	5059.6	1.457	1.652
25R	4994.6	5058.9	0.629	0.563
35R	5023.7	5058.2	-0.035	-0.262
45R	5053.1	5057.4	-1.030	-1.007
14R	4965.0	5030.3	1.789	2.522
24R	4994.1	5029.6	1.446	1.712
34R	5023.1	5029.1	-0.426	-0.141
44R	5023.3	5028.4	-1.112	-1.551
13R	4964.1	5001.3	0.965	1.563
23R	4993.3	5000.6	0.756	1.080
33R	5022.4	5000.0	0.044	0.686
43R	5051.4	4999.4	0.102	-0.014
12R	4963.3	4972.0	0.694	1.223
22R	4992.6	4971.4	0.413	0.681
32R	5021.8	4970.8	-0.400	0.745
42R	5050.7	4970.5	0.387	1.240
11R	4963.0	4943.0	1.424	2.291
21R	4991.9	4942.2	0.091	0.692
31R	5021.1	4941.5	-0.606	-0.749
41R	5050.3	4940.8	-1.408	-1.927

NOTE: Z (A) VALUES ARE FROM CONTRACT N66001-84-N0847.  
Z (B) VALUES ARE FROM CONTRACT N66001-84-N0113.  
Z (C) VALUES ARE FROM CONTRACT N66001-84-N0106.

(C) Grid height values in feet  
(not leveled)

Figure 22. Stereo spot height analysis of wake.

directly aft of QUAPAW (model 12) and canted at 15 degrees to match the ship heading across the image.

Table 12. Stereomodels analyzed.

Wake Image	Pass	Model #	Contractor <sup>1</sup>	Approach	Data Points <sup>2</sup>
Metric buoy	DREP 7-1	1	A	Stereo orientation for scale (3)	42
			B	Not reported	0
			C	Contour plot	2500
Stbd Wake 12.6°	DREP 7-1	9	A	Spot readings on grid	2562
			B	Profiles	5473
			C	Stereomodel setup only	15
Center-line & Stern QUAPAW	DREP 7-1	12	A	Contour plot	5086
			A	Stereo orientation for scale (3)	75
			A	Spot readings on QUAPAW stern	150
			A	Wake profiles behind QUAPAW	268
			B	Profiles on grid	6596
			C	Contour plot	400
			C	Spot readings on grid	300
Port near ship	DREP 8-3	16 <sup>3</sup>	A	Spot readings on grid	1639
			B	Profiles	5473
			C	Orientations for <u>study</u> (2)	30
				Total points	34000 <sup>4</sup>

1. Each contractor also sent written report/data summary.
2. In addition, between 15 and 45 Reseau reference grid points read per model.
3. Model 16 was only usable over half its area due to cloud reflections.
4. The cost to analyze data in \$ per 1000 points was: (A) 214, (B) 200, and (C) 194.

In order to have a common data set for each model from three contractors, the fixed Reseau grid pattern appearing in each separate image was chosen to provide common points of measurement under which to determine water surface elevation. Figure 22B shows the grid patterns of both left and right cameras as they appear in the overlap model. These reference grid data from the three contractors for model 9 are shown in figure 22C. To obtain this data each company arrived at their own set of spatial parameters. Figure 23A gives a comparison of three values: the baseline ( $\Delta Y$ ), tilt of the aircraft ( $\Delta Z$ ), and left-right orientation angle differences ( $\Delta w$ ,  $\Delta \phi$ ,  $\Delta \kappa$ ).

The convergence ( $\Delta \phi$ ) between the two cameras was set and measured on the ground at  $5 \pm 0.5$  degree. The rotation ( $\Delta \kappa$ ) was initially estimated from the photos at 1.5 degrees. The third angle ( $\Delta w$ ) measures how far the axis of one camera leads the other along the flight direction. Extraction of this setting from the image is partially hidden in forward blur caused by aircraft motion during the minimum exposure (1/500th second  $\sim 10$  cm on the ground). Some variation between contractors exists for this set-up value but this parameter is not in the parallax direction and does not affect the metric solution for rigidly mounted cameras with synchronized shutters.

These frames were selected for analysis in the absence of positioning data. Now that precise positions are available (Hughes, 1984), this method, complemented and compared with stereo measurements, will be employed further back in the wake where photographic roughness within individual SAR resolution cells can be compared with SAR image intensity.

#### STEREO MENSURATIONS

Using an airborne stereo photogrammetric approach is the only known way to extract instantaneous sea surface topography with fine height resolution over even a moderately large area, as shown in Pierson (1976). The need for precise mapping of small waves in a ship wake with centimeter height resolution causes a drastic revision of any of the previous mapping approaches, such as used by the Stereo Wave Observation Project (SWOP) conducted from 1954 to 1960, (Cote, 1960). Instead of two widely separated photo aircraft operating at 1000-2000 meters altitude, for the JOWIP experiment, a unique configuration was created for use at heights between 15-75 meters. Rigidly mounting two identical motor-drive cameras in the wing-tip tank fairings of a single aircraft, a fixed-baseline system was created with a separation of 10.7 meters. With accurate knowledge of this fixed-baseline, we avoided almost all work and problems associated with pitch, roll, and yaw determination and ground control surveying.

As substantiated by an expert in fixed-baseline photogrammetry (Kenefick 1984), for adequate reconstruction of the scene in an analytical stereo plotter and extraction of relative height data, only the camera separation and approximate altitude need be known in the rigid stereo camera system created by NOSC. The only ground support needed is a calibrated horizontal distance in a few photo frames to serve as metrics for horizontal scale. During JOWIP, three such metrics were used as "floating" ground control: (1) a tri-spar buoy photographed on each major flight pass with an 8-meter triangular pattern, (2) grid marks on the stern helicopter deck of the CFAV ENDEAVOUR, and (3) QUAPAW's existing aircraft operations pattern at the stern.

Table 12 summarizes the initial set of data produced by three independent photogrammetric contractors using the highly versatile features of computer-controlled analytic stereoplotters. Note that the model frame numbers are on different runs than previous calm-water examples. Since there is a variety of possible ways to select, analyze, and display height topography from stereo image pairs (called stereomodels), three basic approaches were used: contour plot, spot-height reading, and the directed profile method. A continuous analysis method, along paths of apparent equal height, produces the contour plot, and the output resembles familiar topographic maps. This approach is good for preliminary study, but any attempt to manipulate or level the data set for comparison purposes would require vast amounts of computer time and multiple assumptions. For this reason the other two methods are more directly suitable for analysis. The spot-height method takes height data off stereomodels only at predetermined points, usually on equal grid spacing. Such an approach is shown applied to model 9 in figure 22A and a resultant three-dimensional plot can be seen in figure 23C. The profile approach is the most efficient and also uses spot height measurement techniques but along lines across the image optimally oriented to the wavelength outputs desired. An example profile set is shown in figure 23D, where cross-sectional slices were

The shift from shorter wavelengths at small wake angles to longer wavelengths at wider angles is apparent but complicated by the additional variables of distance aft and phase on the transverse wave. While the wavelength bin centered on 30 cm shows maximum enhancement near the predicted 2.5-degree wake angle, the 70-cm wavelength bin displays much higher enhancement for all angles from the wake centerline to 3.0 degrees. For larger wake angles, image power is generally depleted in both these shorter wavelength lines with enhancement at the longer wavelengths.

Image power propagation direction variation shows a large increase in the cross-track direction ( $90^\circ$ ). Power in the cross-track bin was summed over a 30-degree sector between 75 and 105 degrees relative to the QUAPAW heading. Unfortunately the sun azimuth was 107 degrees relative at the time of this photo. But the critical angle from table 10 shows that a 40-degree slope would be required for direct sun reflection. While this increase is not present in the background areas, the tilt of the longer transverse waves is thought to combine with an increase in the otherwise uniform sky radiance near the sun, resulting in a nonlinear enhancement. Nonetheless, comparison of the 90-degree bin with the 120-degree bin which includes the sun azimuth, clearly indicates a large increase in image power in the cross-track ( $90^\circ$ ) direction.

In figure 21 the FFT image power in the cross-track direction ( $\pm 15^\circ$ ) is shown for the two shorter wavelength lines. The 70 cm plot shows power spread along the 3.6-degree wake angle measured on the SAR image (table 9), but the 30-cm enhancement is limited to the area between 200 and 300 meters aft. While these data clearly indicate large increases in the short wavelengths present along the narrow wake angles, they do not allow us to select between first (30 cm) and second (60 cm) Bragg resonant scattering, nor for that matter, specular reflection from the ship disturbed water surface.

LEGEND:

- < 1 Std. Dev (Above Background)
- > 1
- > 2
- > 3
- △ > 6
- > 12

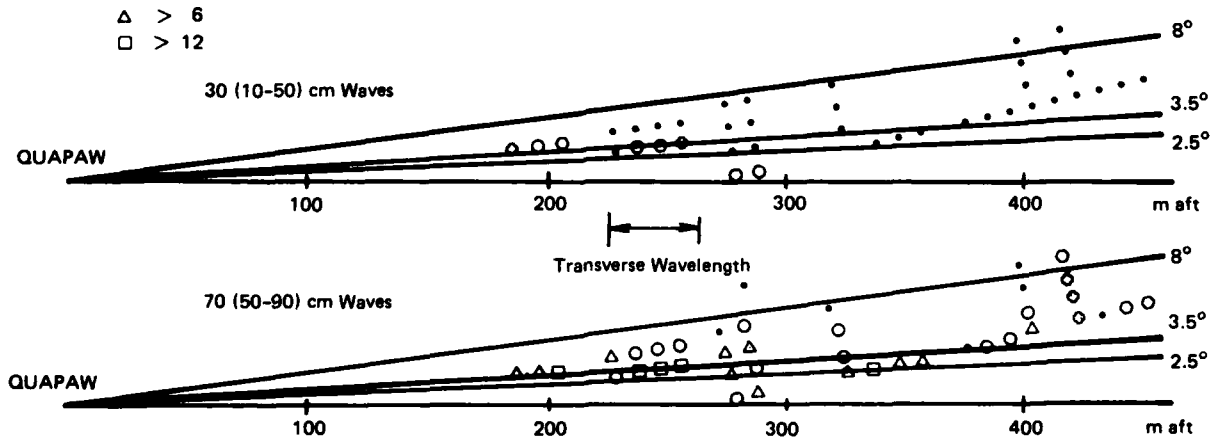


Figure 21. Standard deviations above background for cross-track propagating waves.

In this representative example we see that the image power has been drastically shifted from the longer to the shorter wavelength bins. The maximum image power now exists in the 0.5- to 0.9-meter annulus rather than the 1.4- to 10-meter annulus. The direction of this strong trend is uncomfortably close (120° relative) to the azimuth of the sun (107° relative) and aft of any ship-induced stationary Kelvin pattern components.

Table 11 shows the variation of total power (expressed in standard deviations above background) with wake angle as a function of wavelength (all directions) and propagation direction (all wavelengths). The average theoretical Kelvin wake angles corresponding to each wavelength bin are 2.5, 3.8, 4.9, and 10.7 degrees, respectively. Kelvin wake wavelengths for the first three propagation direction bins would be 40, 30, and 10 meters, respectively; hence showing very low power in a 10 x 10 meter image. The wavelength approaches zero in the cross-track direction where most of the power is shown, and there should be no components of the stationary Kelvin pattern abaft the beam.

Table 11. Total image power variation as a function of wake angle, wavelength, and propagation direction (Run 8-3); standard deviations above background.

FFT #	Wake Angle	Distance Aft	Wavelength (cm)					Propagation Direction (deg)				
			30	70	120	570	0	30	60	90	120	150
247	0.2	289	2.9	12.6	-0.5	-1.9	2.5	-4.6	-1.9	4.0	3.1	2.3
243	0.6	280	3.3	10.5	-2.1	-0.5	2.5	-5.6	-2.3	1.2	0.2	12.2
244	1.4	277	-0.2	8.9	-0.0	-1.4	-0.8	-4.8	-0.7	11.3	3.7	-0.7
224	1.4	326	-0.8	2.7	1.9	-1.8	-1.6	-6.3	-1.6	15.2	6.2	0.8
111	1.5	228	0.0	1.6	-3.2	2.2	-2.4	-5.1	-2.3	5.0	12.6	-0.2
228	1.7	338	-0.6	5.7	2.8	-3.0	-0.8	-5.9	-2.3	11.8	7.0	2.2
248	1.8	287	-0.4	9.9	1.2	-2.5	-1.7	-4.9	-1.3	18.8	3.1	-0.4
113	1.9	237	1.3	17.5	0.2	-3.1	-2.1	-6.1	-1.9	10.9	6.0	6.0
105	2.0	187	0.9	3.5	-2.2	1.1	-1.3	-6.4	-1.6	18.1	2.3	4.7
229	2.1	347	-1.0	3.6	1.1	-1.3	-0.6	-4.5	-1.4	19.5	1.9	-8.1
115	2.2	248	0.9	11.1	0.2	-2.1	-2.3	-4.6	-1.8	11.9	6.6	1.8
230	2.3	357	-1.0	5.7	0.5	-1.2	-2.0	-4.8	-0.6	13.0	4.2	-0.2
107	2.4	197	1.8	6.2	-2.6	0.7	-2.1	-5.6	-1.8	16.2	4.6	3.5
117	2.5	257	0.4	15.4	1.4	-3.6	-2.9	-5.6	-0.9	24.7	4.2	-3.5
109	2.8	206	1.1	8.9	-1.7	-0.3	-2.8	-6.4	-1.0	23.3	3.4	0.4
214	2.9	376	-1.3	-1.6	-1.2	1.3	-2.1	-6.2	1.7	19.0	-0.2	-3.3
225	3.1	325	-0.8	0.2	0.8	-0.6	-2.7	-6.1	-0.5	25.1	2.9	-3.2
231	3.3	386	-1.1	-0.2	0.0	0.1	-2.1	-5.7	-1.5	30.3	2.1	-3.6
245	3.4	275	-1.4	1.0	-0.9	0.7	-1.1	-6.1	-2.8	26.0	5.0	-1.8
232	3.4	395	-1.3	-0.9	0.5	-0.1	-2.1	-5.2	1.0	20.9	-0.1	-4.1
249	3.7	285	-0.9	2.4	-1.0	0.5	-0.4	-2.1	-2.5	18.0	2.1	-2.1
233	3.7	405	-1.3	0.9	-0.4	0.3	-2.3	-5.1	-1.1	31.1	-1.2	-1.1
139	3.9	227	-0.4	1.5	1.4	-1.2	-2.7	-7.1	-1.7	27.1	5.3	-1.6
200	4.0	424	-1.3	-2.9	-3.7	3.4	-1.7	-6.1	-0.8	34.3	-0.2	-5.6
141	4.1	236	-0.6	-0.2	2.7	-1.9	-3.0	-7.4	-2.2	36.5	2.0	0.6
204	4.3	434	-1.3	-2.3	-3.3	3.0	-3.0	-6.2	-2.0	36.3	2.5	-4.9
143	4.4	246	-0.3	-0.4	0.2	-0.1	-2.5	-6.6	-0.3	24.9	3.0	-2.9
145	4.6	225	-1.0	-0.7	0.0	0.2	-2.7	-6.7	-0.6	29.7	0.5	-0.8
205	4.5	443	-1.3	-2.6	-3.2	3.0	-2.4	-5.8	-2.9	46.5	-0.3	-5.1
206	4.6	453	-1.2	-2.8	-3.3	3.1	-2.2	-5.6	-2.4	30.7	5.2	-5.1
226	4.8	323	-0.2	0.3	-1.9	1.4	-1.6	-4.5	-1.4	25.5	0.6	-1.6
234	5.0	403	-1.3	2.2	-1.6	1.1	-0.7	-4.1	0.5	9.9	0.8	-0.9
246	5.4	273	-1.2	-3.8	-4.0	3.8	-2.6	-7.1	-3.3	52.4	0.1	1
201	5.4	422	0.4	0.2	-2.2	1.6	-0.8	-5.9	-0.9	24.2	0.5	-1.4
250	5.7	283	-0.6	0.2	-2.5	1.9	-1.4	-4.5	-2.6	25.7	2.2	-0.4
215	6.5	400	-1.5	-2.1	-3.2	2.9	-2.2	-4.0	0.9	18.0	-0.4	-2.9
227	6.6	321	-0.1	-0.5	-2.7	2.2	-2.2	-2.1	0.5	9.7	-0.4	0.6
202	6.7	419	-0.1	0.4	-2.0	1.5	-0.6	-2.6	-2.0	16.8	-1.4	4.4
216	7.9	398	-1.3	0.1	-2.3	1.9	-1.0	0.2	-0.7	0.5	3.6	-1.4
203	8.0	417		1.4	0.9	-1.4	0.7	0.2	-4.3	0.6	8.5	-0.6

Image power in four directional wave number bins in each of six directions relative to the QUAPAW track was then summed and expressed as a percent of the total image power. An example of this for an FFT of an area at a 2.2-degree wake angle, 248 meters aft of the ship, number 115 from photo frame 13 is shown to the left in figure 20.

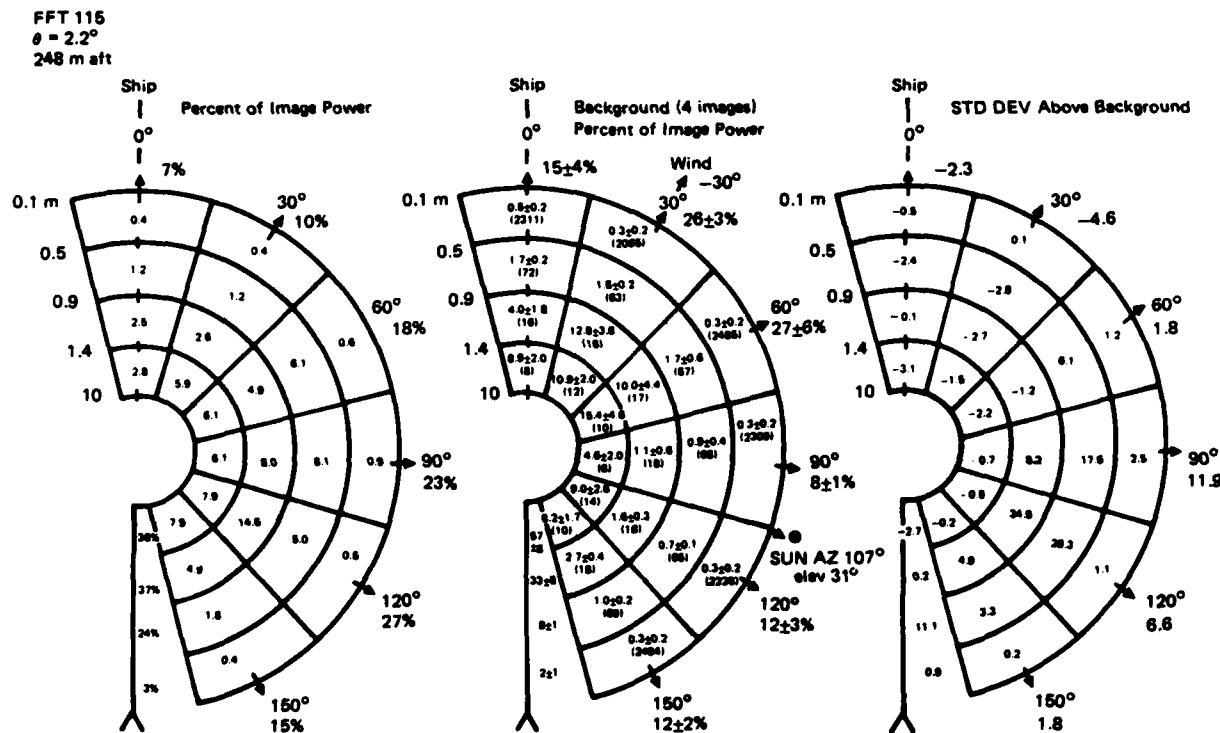


Figure 20. Image power (%), background (%), and image (std. dev. above background), binned by wavelength (m) and propagation direction (deg).

An identical procedure was performed on the four background areas shown and the resulting statistics (mean, standard deviation on number of points) are shown for each bin in the center of figure 20. Total percents are also shown for each direction (sector) and wavelength bin (annular ring). The background statistics reveal predominant image power in the general direction (30° relative) of the surface wind (2.6 m/s). The highest power is found in the 1.4- to 10-meter wavelength bins as would be predicted (6.5 m) for this wind speed.

After the variations in total image power between FFTs had been removed by the use of percentages, the percent in each wavelength-direction bin was expressed in standard deviations above or below background for comparison purposes. The diagram on the right of figure 20 is an example of this procedure.

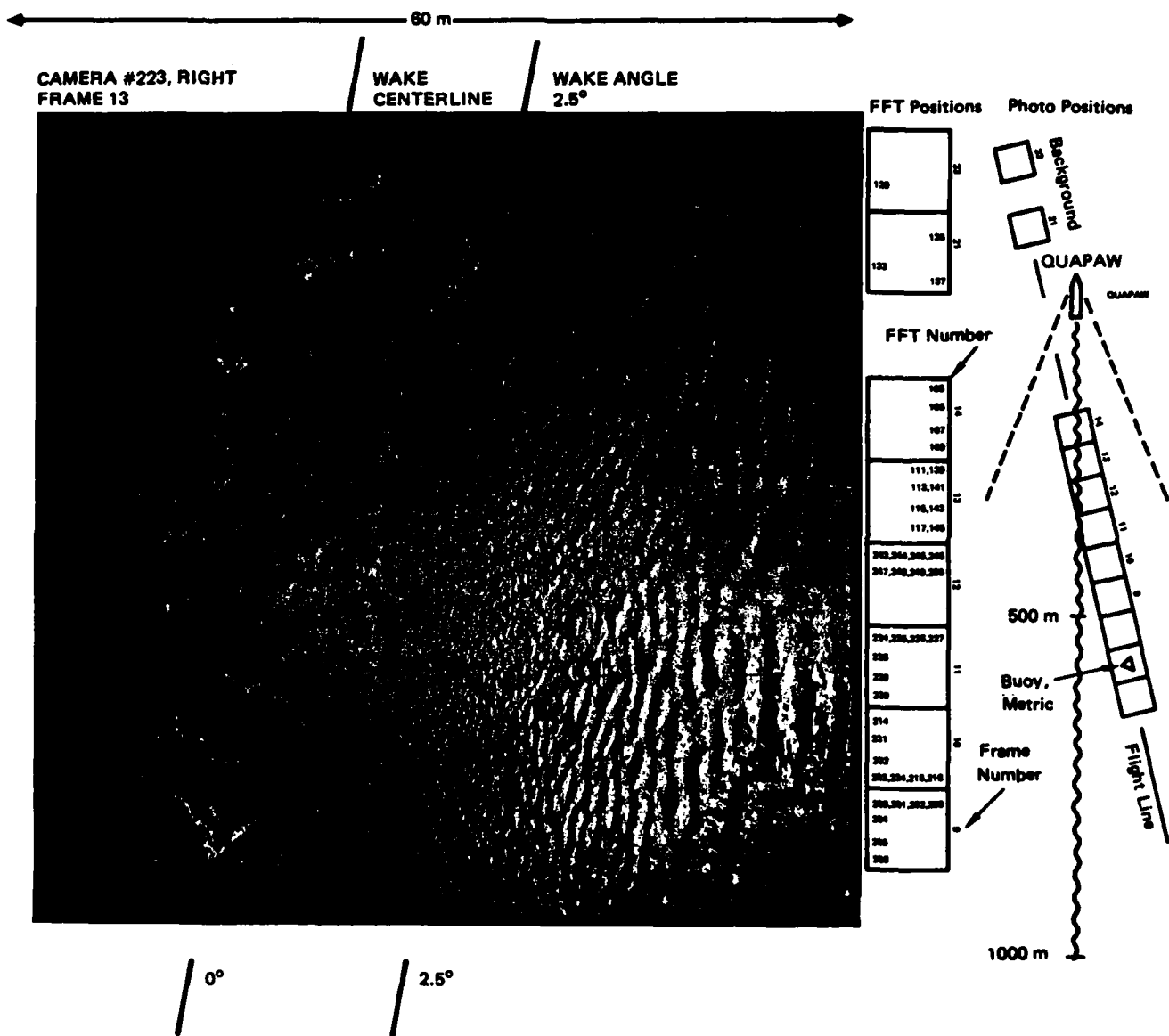


Figure 19. Location of FFT areas in wake with photo example.

## CONCLUSIONS AND RECOMMENDATIONS

Conclusions which can be drawn from the above data vary in confidence level and will be presented here highest first, followed by a few suggestions on the application and verification of these concepts in future experiments.

The hypothesized ship-induced surface roughness has been shown to be responsible for the narrow wake angles observed within the classical Kelvin wake envelope on SEASAT-like SAR images. These angles are observed during periods of locally depleted wind wave population: i.e., calm winds in the immediate area of the wake pattern. As the average wind speed increases above 2.5 m/s, narrow wake arm enhancement gives way to a full pattern of transverse waves against the wind-roughened background within the Kelvin vee-envelope on JOWIP L-band images. Above 3.5 m/s only a trace of the turbulent wake is evident and above 9 m/s all wake remnants are obscured.

Measurement of ship-induced surface roughness wavelengths in the areas of maximum SAR modulation along the narrow wake arms in JOWIP images during periods of calm winds are presently insufficient to differentiate between first and second order Bragg scattering. While the data presented here show no indication of specular scattering, better statistics are required to dismiss this mechanism completely.

Photographic observations on calm water reveal substantially increased populations of short gravity wavelengths along the narrow angles of the ship wake corresponding to strong SAR modulations (14 dB). These modulations are roughly spaced along track at the maximum transverse wake component wavelength and produce the largest SAR image modulation at azimuth ship headings. This intense modulation for azimuth-traveling transverse waves strongly suggests that an orbital motion mechanism like velocity bunching, as described by Alpers et al., (1979, 1981, 1983), is the response mechanism.

Further analysis of transverse wake, wave amplitude, port-to-starboard wake arm azimuth offset and smear may provide important additional data for evaluating SAR image modulation theories. SEASAT observations suggest that long ocean swell may also be made detectable on calm seas through ship-generated roughness over a range of wavelengths and propagation directions, but further analysis of narrow wakes in locally calm wind areas on SEASAT images is required to substantiate this hypothesis.

The combination of the long transverse wave train and cross-track short gravity wave Bragg roughness that a ship produces during calm wind conditions, provides the ideal controlled surface conditions essential for SAR image modulation experiments. It is therefore recommended that further experiments exploiting this method be performed to provide data for theoretical SAR modeling. In each such experiment, after the baseline case (displaying a narrow transverse wave modulated wake for an azimuth traveling ship on calm water) has been demonstrated, the effects of transverse wave direction (ship heading), wavelength (ship speed), and incidence/scattering mechanism (ship

locations in the swath) under increasing background wind conditions can be quantitatively evaluated. Images collected in this manner, when combined with simultaneous photographic records of surface conditions and ambient wind and surface wave spectral measurements, can provide the data essential for quantitative comparison of SAR ocean wave imaging theories.

#### REFERENCES

- Alpers, W.R. and C.L. Rufenach. "The Effects of Orbital Motions on Synthetic Aperture Radar Imaging of Ocean Waves." IEEE Transactions on Antennas Propagation, 1979, AP-27, 685-690.
- Alpers, W.R., D.B. Ross, and C.L. Rufenach. "On the Detectability of Ocean Surface Waves by Real and Synthetic Aperture Radar," Journal of Geophysical Research, 1981, 86, 6481-6498.
- Alpers, W.R. "Monte Carlo Simulations for Studying the Relationship Between Ocean Wave and Synthetic Aperture Image Spectra." Journal Geophysical Research, 1983, 88, 1745-1759.
- Cote, L.J., J.O. Davis, W. Marks, R.J. McGough, E. Mehr, W.J. Pierson, J.F. Ropek, G. Stephenson and R.C. Vetter. "The Directional Spectrum of a Wind Generated Sea as Determined from Data Obtained by the Stereo Wave Observation Project." Meteorol. Paper, Vol. 2, No. 6, New York University Press, New York, June 1960.
- Cox, C., and W.H. Munk. "Statistics of the Sea Surface Derived from Sun Glitter," Journal Marine Research, 1954, 13(2), 198-227.
- Fu, L.L., and B. Holt. "SEASAT Views Oceans and Sea Ice with Synthetic Aperture Radar," Publication 81-120, Jet Propulsion Laboratory, Pasadena, CA, Feb 15, 1982.
- Hager, R.O. "The side-looking radar image of time-variant scenes," Radio Science, 1980, 15, (4), 749-756.
- Havelock, T.H. "Wave Patterns and Wave Resistance," Trans. INA, 1934 74, 430-442.
- Hughes, B.A. Private Communication, "Internal Waves in Dabob Bay During JOWIP", 7 Nov 1983.
- Hughes, B.A. Private Communication, "QUAPAW Speeds, Headings and ENDEAVOUR Wake Crossing (3°) Times", 25 Apr 1984.
- Hulbert, F.O. "The Polarization of Light at Sea," Journal of the Optical Society of America, 1934, 24, (35).
- Inui, T. "Wave-Making Resistance of Ships," Trans. Soc. Nav. Arch. Engr., 1962, 70, 283.

Keller, W.C. and J.W. Wright. "Microwave Scattering and the Straining of Wind-Generated Waves," *Radio Sci.*, 1975, 10, 139-1947.

Kenefick, J.F. "Analytical Study of Ocean Waves and Ship Wakes Using Airborne Stereo Photogrammetry." Letter Report, Contract No. N66001-84-M-0113, 6 June 1984.

Lighthill, J. "Waves in Fluids," New York, Cambridge University Press, 1978.

Munk, W.H. "Kelvin-Wake-Dabob Bay," in *JASON SEASAT III and IV*, Aug 1984, Mitre Corp. JSR-84-203, 3-1 to 3-15.

Pierson, W. J. "The Theory and Applications of Ocean Waves Measuring Systems at and Below the Sea Surface on the Land, from Aircraft and from Spacecraft," NASA Rept. CR-26-2646, Contract No. NAS 5-20041, Jan 1976.

Phillips, O.M.M. "The Dynamics of the Upper Ocean," 51-54, 1977, New York. Cambridge University Press.

Shuchman, R.A., and J.S. Zelenka. "Processing of Ocean Wave Data from Synthetic Aperture Radar," *Boundary Layer Meteorol.*, 1978, 13, 181-191.

Shuchman, R.A., "Processing of Synthetic Aperture Radar Data of Ocean Waves, in Oceanography from Space." Ed. J.F.R. Gower, 477-496, 1981, New York, Plenum.

Shuchman, R.A. "Digital Ground Range Corrected SAR Image," JOWIP Run 8-2, June 1984.

Stillwell, Jr., D. "Directional Energy Spectra of the Sea from Photographs," *Journal of Geophysical Research*, 1969, 74, 1974-1986.

Valenzuela, G.R. "Theories for the Interaction of Electromagnetic and Ocean Waves - A Review," *Boundary Layer Meteorol.*, 1978, 13, 61-85.

Vesecky, J.F., and R.H. Stewart. "The Observation of Ocean Surface Phenomena Using Imagery from the SEASAT Synthetic Aperture Radar," *J. Geophys. Res.*, 1982, 87, 3397-3430.

Vesecky, J.F., and R.H. Stewart, R. A. Shuchman, H.M. Assas, F.R. Kasischke, and J.D. Lyden. "On the Ability of Synthetic Aperture Radar to Measure Ocean Waves," Proceedings of the IUCRM Symposium on Wave Dynamics and Radio Probing of the Ocean Surface, O.M. Phillips, editor, Sept 1982.

Webster, W.D. "Private Discussions on Ship Wake Structures," Dept. of Naval Architecture, Univ. of Calif., Berkeley, 5 Aug 1982.

Wright, J.W. "A New Model for Radar Sea Clutter," IEEE Transactions on Antennas and Propagation, 1968 AP-16, 217-223.

Wright, J.W., W.J. Plant, and W.C. Keller. "Ocean Wave-Radar Modulation Transfer Functions from the West Coast Experiment," Journal of Geophysical Research, 1980, 85 4957-4966.

## APPENDIX A - AVAILABLE DIGITAL DATA

There are three categories of digital data; time series, track, and image — all are recorded on 9-track 1600 BPI digital tape.

The time series data and track are both stored in VAX/VMS FILES-II level 2 direct access files and may be read from tape using the VMS "COPY" command. The images are stored integer\*2 with one row per record.

### A-1 TRACK DATA

SAR RUN	Vessel	Start	Stop
5/3	ENDEAVOUR	09:51:03	10:38:13
	QUAPAW	09:58:32	10:34:48
	CESSNA	10:17:30	10:38:09
5/4	ENDEAVOUR	10:42:34	11:31:36
	QUAPAW	10:43:03	11:31:36
	CESSNA	10:43:01	11:21:40
6/1, 2, 3	ENDEAVOUR	14:44:35	16:18:56
	QUAPAW	14:44:44	16:18:54
	CESSNA	15:21:53	16:18:56
6/4	ENDEAVOUR	16:22:31	17:56:04
	QUAPAW	16:22:19	17:04:06
	CESSNA	16:22:32	16:56:27
	ENDEAVOUR	14:57:13	15:18:26
	QUAPAW	14:57:12	15:18:26
7/1, 2, 3, 4	ENDEAVOUR	15:59:12	17:41:01
	QUAPAW	16:52:43	17:41:01
	CESSNA	16:09:31	17:25:09
7/5, 6, 7	ENDEAVOUR	18:13:32	20:00:43
	QUAPAW	18:13:34	10:00:43
	CESSNA	18:13:48	19:47:54
8/1	ENDEAVOUR	07:22:06	07:48:17
	QUAPAW	07:21:57	07:48:16
	CESSNA	07:21:59	07:43:11
8/2	ENDEAVOUR	08:06:17	08:29:21
	QUAPAW	08:06:16	08:29:21
	CESSNA	08:06:16	08:28:28
8/3	ENDEAVOUR	08:48:58	09:14:40
	QUAPAW	08:48:01	09:14:40
	CESSNA	08:50:23	09:08:54
8/4	ENDEAVOUR	09:36:25	09:57:52
	QUAPAW	09:36:29	09:57:41
	CESSNA	09:41:38	09:57:45
	ENDEAVOUR	10:25:43	11:08:39
	QUAPAW	10:25:45	11:08:40
	ENDEAVOUR	11:18:23	11:37:19
	QUAPAW	11:18:20	11:37:20
9/1, 2, 3, 4	ENDEAVOUR	13:02:19	15:05:04
	QUAPAW	13:02:14	15:08:50
	CESSNA	13:03:43	14:55:06

## A-2 TIME SERIES DATA

### PARAMETER

- a. Water velocity measured with respect to the ship expressed as North- and East-going components
- b. Distance the ship has traveled through the water; obtained by integrating the bow current meter signal (meters)
- c. Conductivity, temperature, sigma-t, and depth below the mean sea surface (Siemens/meter) (Degrees C) (Kg/m<sup>3</sup>) (meters)
- d. Time-differentiated wave height (meters/second)
- e. Ships heading (degrees)
- f. Relative wave height (meters)
- g. Mean-square differentiated wave height ((m/s)<sup>2</sup>)
- h. Mean-square wave height (meters squared)
- i. Mean-square wave-slope
- j. Same as a. but measured from stern current meter
- k. Same as b. but measured from stern current meter
- l. Wave-slope, north and east components with laser intensity for each pair of components
- m. Wind velocity (m/s)

Tapes are available for the following SAR runs.

5-3, 5-4, 6-4, 8-1, 8-2, 8-3, 8-4, 9-1, 9-2, and 9-3

## A-3 SAR IMAGES

SAR <u>RUN</u>	<u>Band</u>	<u>Slant</u>	<u>Ground</u>
1-4	L	3200x1600	3200x1994
5-3	L	3600x1800	3600x3152
6-4	X	3600x1800	3600x3442
8-2	L	3200x1550	3200x3942
8-3	L	3600x1800	3600x3494
8-4	L	3600x1800	3600x2654
9-1	L	3200x1600	3200x3584
9-2	L	3200x1600	3200x3964
10-8	L	3200x1600	3200x2566

**APPENDIX B - VERTICAL (STEREO) PHOTO TIMES**

<u>DREP 5-3</u>		<u>DREP 5-4</u>		<u>DREP 6-1</u>	
<u>Run 1</u>		<u>Run 1</u>		<u>Run 1</u>	
<u>Fr#</u>	<u>Time (PDT)</u>	<u>Fr#</u>	<u>Time (PDT)</u>	<u>Fr#</u>	<u>Time (PDT)</u>
1	10:16:29	1	11:01:04	1	15:18:36
2	10:16:30	2	11:01:05	2	15:18:37
3	10:16:31	3	11:01:06	3	15:18:38
4	10:16:32	4	11:01:07	4	15:18:39
5	10:16:33	5	11:01:08	5	15:18:40
6	10:16:34	6	11:01:09	6	15:18:41
7	10:16:35	7	11:01:10	7	15:18:42
8	10:16:36	8	11:01:11	8	15:18:43
9	10:16:37	9	11:01:12	9	15:18:44
10	10:16:38	10	11:01:13	10	15:18:45
		11	11:01:14	11	15:18:46
		12	11:01:15	12	15:18:47
		13	11:01:16	13	15:18:48
		14	11:01:17	14	15:18:49
		15	11:01:18	15	15:18:50
		16	11:01:19	16	15:18:51
				17	15:18:52
		<u>Run 2</u>		18	15:18:53
				19	15:18:54
		<u>Fr#</u>	<u>Time (PDT)</u>	20	15:18:55
		1	11:05:15		
		2	11:05:16		
		3	11:05:17		
		4	11:05:18		
		5	11:05:19		
		6	11:05:20		
		7	11:05:21		
		8	11:05:22		
		9	11:05:23		
		10	11:05:24		
		11	11:05:25		

DREP 6-4

<u>Run 1</u>		<u>Run 2</u>		<u>Run 3</u>	
<u>Fr#</u>	<u>Time (PDT)</u>	<u>Fr#</u>	<u>Time (PDT)</u>	<u>Fr#</u>	<u>Time (PDT)</u>
1	16:44:04	1	16:46:30	1	16:49:35
2	16:44:05	2	16:46:31	2	16:49:36
3	16:44:06	3	16:46:32	3	16:49:37
4	16:44:07	4	16:46:33	4	16:49:38
5	16:44:08	5	16:46:34	5	16:49:39
6	16:44:09	6	16:46:35	6	16:49:40
7	16:44:10	7	16:46:36	7	16:49:41
8	16:44:11	8	16:46:37	8	16:49:42
9	16:44:12	9	16:46:38	9	16:49:43
10	16:44:13	10	16:46:39	10	16:49:44
11	16:44:14	11	16:46:40		
12	16:44:15	12	16:46:41		
13	16:44:16	13	16:46:42		
14	16:44:17	14	16:46:43		
15	16:44:18	15	16:46:44		
16	16:44:19	16	16:46:45	1	16:51:16
17	16:44:20	17	16:46:46	2	16:51:17
18	16:44:21	18	16:46:47	3	16:51:18
19	16:44:22	19	16:46:48	4	16:51:19
20	16:44:23	20	16:46:49	5	16:51:20
21	16:44:24	21	16:46:50	6	16:51:21
22	16:44:25	22	16:46:51	7	16:51:22
23	16:44:26	23	16:46:52	8	16:51:23
24	16:44:27	24	16:46:53		
25	16:44:28	25	16:46:54		
26	16:44:29	26	16:46:55		
27	16:44:30	27	16:46:56		
28	16:44:31	28	16:46:57		
29	16:44:32	29	16:46:58		
30	16:44:33	30	16:46:59		
		31	16:47:00		
		32	16:47:01		
		33	16:47:02		
		34	16:47:03		
		35	16:47:04		
		36	16:47:05		
		37	16:47:06		
		38	16:47:07		
		39	16:47:08		

DREP 7-1DREP 7-3

<u>Run 1</u>		<u>Run 1</u>		<u>Run 1</u>	
<u>Fr#</u>	<u>Time (PDT)</u>	<u>Fr#</u>	<u>Time (PDT)</u>	<u>Fr#</u>	<u>Time (PDT)</u>
1	16:13:09	1	17:13:43	1	17:15:09
2	16:13:10	2	17:13:44	2	17:15:10
3	16:13:11	3	17:13:45	3	17:15:11
4	16:13:12	4	17:13:46	4	17:15:12
5	16:13:13	5	17:13:47	5	17:15:13
6	16:13:14	6	17:13:48	6	17:15:14
7	16:13:15	7	17:13:49	7	17:15:15
8	16:13:16	8	17:13:50	8	17:15:16
9	16:13:17	9	17:13:51	9	17:15:17
10	16:13:18	10	17:13:52	10	17:15:18
11	16:13:19	11	17:13:53	11	17:15:19
12	16:13:20	12	17:13:54	12	17:15:20
13	16:13:21	13	17:13:55	13	17:15:21
14	16:13:22	14	17:13:56		
15	16:13:23	15	17:13:57		
16	16:13:24	16	17:13:58		
17	16:13:25	17	17:13:59		
18	16:13:26	18	17:14:00		
19	16:13:27	19	17:14:01		
20	16:13:28	20	17:14:02		
21	16:13:29	21	17:14:03		
22	16:13:30	22	17:14:04		
23	16:13:31	23	17:14:05		
24	16:13:32	24	17:14:06		
25	16:13:33	25	17:14:07		
26	16:13:34	26	17:14:08		
27	16:13:35				

DREP 7-5DREP 7-7

<u>Run 1</u>	
<u>Fr#</u>	<u>Time (PDT)</u>
1	18:24:18
2	18:24:19
3	18:24:20
4	18:24:21
5	18:24:22
6	18:24:23
7	18:24:24
8	18:24:25
9	18:24:26
10	18:24:27
11	18:24:28
12	18:24:29
13	18:24:30
14	18:24:31
15	18:24:32
16	18:24:33
17	18:24:34
18	18:24:35
19	18:24:36
20	18:24:37
21	18:24:38
22	18:24:39
23	18:24:40
24	18:24:41
25	18:24:42
26	18:24:43
27	18:24:44
28	18:24:45
29	18:24:46
30	18:24:47
31	18:24:48
32	18:24:49
33	18:24:50
34	18:24:51
35	18:24:52
36	18:24:53
37	18:24:54
38	18:24:55
39	18:24:56
40	18:24:57
41	18:24:58
42	18:24:59
43	18:25:00

<u>Run 1</u>	
<u>Fr#</u>	<u>Time (PDT)</u>
1	19:33:19
2	19:33:20
3	19:33:21
4	19:33:22
5	19:33:23
6	19:33:24
7	19:33:25
8	19:33:26
9	19:33:27
10	19:33:28
11	19:33:29
12	19:33:30
13	19:33:31
14	19:33:32
15	19:33:33
16	19:33:34
17	19:33:35
18	19:33:36
19	19:33:37
20	19:33:38
21	19:33:39
22	19:33:40
23	19:33:41
24	19:33:42
25	19:33:43
26	19:33:44
27	19:33:45
28	19:33:46
29	19:33:47
30	19:33:48

DREP 8-1

<u>Run 1</u>	
<u>Fr#</u>	<u>Time (PDT)</u>
1	07:29:53
2	07:29:54
3	07:29:55
4	07:29:56

Run 2

<u>Fr#</u>	<u>Time (PDT)</u>
1	07:32:30

DREP 8-2

1	8:14:41
2	8:14:42
3	8:14:43
4	8:14:44
5	8:14:45
6	8:14:46
7	8:14:47
8	8:14:48
9	8:14:49
10	8:14:50
11	8:14:51
12	8:14:52
13	8:14:53
14	8:14:54
15	8:14:55
16	8:14:56
17	8:14:57
18	8:14:58
19	8:14:59
20	8:15:00
21	8:15:03
22	8:15:04
23	8:15:05
24	8:15:06
25	8:15:07
26	8:15:08

DREP 8-3

<u>Run 1</u>	
<u>Fr#</u>	<u>Time (PDT)</u>
1	8:59:56
2	8:59:57
3	8:59:58
4	8:59:59
5	9:00:00

Run 2

<u>Fr#</u>	<u>Time (PDT)</u>
8	9:00:03
9	9:00:04

1	10
11	9:00:06
12	9:00:07

13	9:00:08
----	---------

Run 2

<u>Fr#</u>	<u>Time (PDT)</u>
1	9:03:26

DREP 8-4

<u>Run 1</u>	
<u>Fr#</u>	<u>Time (PDT)</u>
1	9:46:21
2	9:46:22
3	9:46:23
4	9:46:24
5	9:46:25

Run 2

6	7
8	9:46:26
9	9:46:27

10	11
11	9:46:31
12	9:46:32

13	14
14	9:46:34

15	16
16	9:46:35
17	9:46:36

18	19
19	9:46:39
20	9:46:40

21	22
22	9:46:42
23	9:46:43

24	25
25	9:46:45
26	9:46:46

27	28
28	9:46:48
29	9:46:49

30	31
31	9:46:51
32	9:46:52

33	34
34	9:46:54
35	9:46:55

36	37
37	9:46:57
38	9:46:58

39	40
40	9:47:00

Run 2

<u>Fr#</u>	<u>Time (PDT)</u>
1	8:17:33

Run 2

<u>Fr#</u>	<u>Time (PDT)</u>
1	9:49:03

DREP 9-1\*Run 1

<u>Fr#</u>	<u>Time (PDT)</u>
16	13:15:36
17	13:15:38
18	13:15:40
19	13:15:42
20	13:15:44
21	13:15:46
22	13:15:48
23	13:15:50
24	13:15:52
25	13:15:54
26	13:15:56
27	13:15:58
28	13:16:00
29	13:16:02
30	13:16:04
31	13:16:06
32	13:16:08

Additional  
Intervals

<u>Fr#</u>	<u>Time (PDT)</u>
1-14	13:13:59
	13:13:25
16-32	13:15:36
	13:16:12
35-48	13:17:07
	13:17:39
49-67	13:18:26
	13:19:04

\*Single color frames  
from 750' alt.

DREP 9-3Run 1

<u>Fr#</u>	<u>Time (PDT)</u>
1	13:59:12
2	13:59:13
3	13:59:14
4	13:59:15
5	13:59:16

Run 2

<u>Fr#</u>	<u>Time (PDT)</u>
1	14:01:19
2	14:01:20
3	14:01:21
4	14:01:22
5	14:01:23
6	14:01:24
7	14:01:25
8	14:01:26
9	14:01:27
10	14:01:28
11	14:01:29

Run 2

<u>Fr#</u>	<u>Time (PDT)</u>
1	14:46:04
2	14:46:05
3	14:46:06
4	14:46:07

<u>Fr#</u>	<u>Time (PDT)</u>
1	14:48:16
2	14:48:17
3	14:48:18
4	14:48:19
5	14:48:20
6	14:48:21
7	14:48:22
8	14:48:23
9	14:48:24
10	14:48:25
11	14:48:26
12	14:48:27

DREP 9-4Run 1

<u>Fr#</u>	<u>Time (PDT)</u>
1	14:45:02
2	14:45:03
3	14:45:04
4	14:45:05
5	14:45:06
6	14:45:07
7	14:45:08
8	14:45:09
9	14:45:10
10	14:45:11
11	14:45:12
12	14:45:13
13	14:45:14
14	14:45:15
15	14:45:16
16	14:45:17
17	14:45:18
18	14:45:19
19	14:45:20
20	14:45:21
21	14:45:22
22	14:45:23
23	14:45:24
24	14:45:25
25	14:45:26
26	14:45:27
27	14:45:28
28	14:45:29
29	14:45:30
30	14:45:31
31	14:45:32
32	14:45:33
33	14:45:34
34	14:45:35

**APPENDIX C - DREP OBLIQUE PHOTO TIMES**

**JULY 26**

ROLL NUMBER 5 RUN 6-1	15:01:07	15:01:40	14:49:40*	14:59:42	15:00:24
	15:10:45	15:11:01	15:13:49	15:09:17	15:09:26
	15:14:11	15:14:18	15:14:51	15:13:56	15:14:04
	15:23:21	15:23:28	15:23:35	15:23:42	15:23:12
	15:23:59	15:24:08	15:24:25	15:24:31	15:23:50
	15:24:54	15:25:02	15:25:24	15:25:36	15:24:41
	15:25:53	15:26:03	15:26:12	15:26:51	15:25:43
	15:27:50				15:27:42

ROLL NUMBER 7	15:29:24	15:29:40	15:30:02	15:30:33	15:30:45
	15:30:52	15:31:06	15:32:59	15:33:07	15:35:11

	15:37:56	16:24:34	16:24:59	16:33:07	16:34:03
RUN 5-4	16:39:50	16:40:05	16:40:30	16:41:01	16:41:29
	16:41:34	16:41:49	16:42:05	16:42:22	16:43:04
	16:43:13	16:43:26	16:43:34	16:43:42	16:43:50
	16:45:15	16:45:20	16:45:35	16:46:43	16:46:58
	16:47:11	16:47:49	16:48:23	16:48:40	16:48:52
	16:49:37	16:49:55	16:50:10	16:50:16	16:50:24
	16:50:37	16:51:14	16:51:23	16:51:31	16:51:53
	16:52:00	16:52:10	16:52:26	16:52:33	16:52:39
	16:52:50	16:52:57	16:53:08	16:53:18	16:53:25
	16:54:17	16:54:28	16:55:32	16:55:40	16:55:47
	16:55:54	16:56:01	16:56:09	16:56:17	16:56:25
	16:56:33	16:56:39	16:56:47	16:57:00	

**JULY 27**

ROLL NUMBER 8 RUN 7-1	16:08:56	16:09:57	16:10:09	16:10:53	16:11:25
	16:12:08	16:12:18	16:12:26	16:12:35	16:12:43
	16:12:51	16:12:58	16:13:51	16:14:37	16:15:14
	16:15:20	16:16:28	16:16:41	16:17:39	16:19:08
	16:19:37	16:20:13	16:20:47	16:21:16	17:10:49

RUN 7-3	17:11:42	17:12:05	17:12:28	17:12:36	17:12:44
	17:12:57	17:13:05	17:13:15	17:13:26	17:13:32
	17:13:40	17:14:25	17:14:39	17:14:52	17:15:00
	17:15:37	17:16:30	17:16:36	17:16:56	17:17:07
	17:17:25	17:17:36	17:18:28	17:18:50	17:19:15
	17:19:34	17:19:49	17:20:10	17:20:35	17:20:40
	17:20:48	17:20:57	17:21:17	17:21:35	17:21:55
	17:22:55	17:23:05	17:24:06	17:24:14	17:25:16
	17:25:22	17:25:30	17:25:38	18:08:41	18:10:09

ROLL NUMBER 9	18:10:18	18:12:47	18:12:55	18:13:16	18:13:48
	18:15:30	18:16:08	18:16:52	18:18:31	18:18:40
	18:18:45	18:22:09	18:22:21	18:22:37	18:22:48
	18:22:57	18:23:05	18:23:12	18:23:20	18:23:27

RUN 7-5	18:23:39	18:23:46	18:23:54	18:24:01	18:24:10
	18:24:20	18:24:35	18:24:43	18:25:03	18:25:40
	18:26:11	18:26:18	18:27:06	18:28:00	18:28:16
	18:28:35	18:29:05	18:30:50	18:31:10	18:31:18
	18:31:41	18:32:05	18:32:34	18:32:40	18:32:49

	18:33:17	18:33:23	18:33:33	18:33:41	18:33:56
	18:34:09	18:34:37	18:34:54	18:35:10	18:35:25
	18:35:57	18:37:13	18:43:53	18:44:00	18:44:08

	18:44:20	18:47:54	18:48:09	19:39:47	19:41:09
RUN 7-7	19:41:14	19:41:24	19:41:31	19:41:41	19:41:54
	19:42:00	19:42:06	19:42:19	19:42:29	19:42:42

JULY 28	7:06:52	7:09:33	7:12:48	7:23:26	7:24:29
ROLL NUMBER 10	7:25:36	7:25:47	7:26:04	7:26:52	7:27:00
RUN 8-1	7:27:17	7:27:23	7:27:31	7:27:39	7:27:48
	7:28:01	7:28:32	7:29:41	7:32:41	7:33:12
	7:34:41	7:35:06	7:35:23	7:35:37	7:40:12
	7:41:13	8:04:17*	8:10:07	8:11:43	8:11:53
	8:12:02	8:12:10	8:12:19	8:12:28	8:12:38
	8:12:48	8:12:59	8:13:10	8:13:21	8:15:07
	8:15:33	8:16:31	8:17:04	8:17:33	8:18:48
RUN 8-2	8:19:09	8:19:24	8:19:33	8:19:43	8:19:59
	8:20:10	8:20:32	8:20:57	8:21:09	8:21:41
	8:22:33	8:22:48	8:22:58	8:24:03	8:24:59
	8:56:36	8:56:46	8:57:24	8:57:51	8:57:59
	8:58:05				
ROLL NUMBER 11	8:59:14	8:59:21	8:59:31	8:59:39	8:59:56
	9:00:02	9:00:40	9:00:49	9:01:01	9:01:16
RUN 8-3	9:02:22	9:02:39	9:02:48	9:02:55	9:03:10
	9:03:32	9:03:41	9:03:50	9:04:08	9:04:43
	9:05:06	9:05:14	9:05:24	9:05:31	9:05:41
	9:06:07	9:06:14	9:06:21	9:06:37	9:06:46
	9:06:54	9:07:04	9:07:12	9:07:20	9:07:29
	9:07:48	9:08:19	9:08:42	9:49:08	9:49:14
	9:49:24	9:50:06	9:50:19	9:50:27	9:50:33
	9:50:40	9:50:47	9:50:56	9:51:08	9:51:16
	9:51:23	9:51:30	9:51:36	9:51:43	9:51:50
RUN 8-4	9:51:58	9:52:07	9:52:14	9:52:26	9:52:58
	9:53:06	9:53:15	9:53:21	9:53:47	9:53:54
	9:54:01	9:54:08	9:54:15	9:54:31	9:54:52
	9:54:57	9:55:05	9:55:17	9:55:26	9:55:35
	9:55:45	9:55:52	9:56:00	9:56:16	9:56:31
ROLL NUMBER 12	13:09:33	13:09:49	13:10:43	13:10:51	13:11:21
	13:11:40	13:12:47	13:12:55	13:13:48	13:13:59
	13:14:19	13:14:32	13:14:48	13:15:00	13:15:22
RUN 9-1	13:15:35	13:15:57	13:16:38	13:16:45	13:16:57
	13:17:13	13:17:24	13:17:31	13:17:57	13:18:07
	13:18:18	13:18:30	13:18:45	13:18:56	13:19:49
	13:20:17	13:20:37	13:21:02	13:22:02	13:53:04
	13:53:15	13:53:52	13:54:21	13:55:23	13:55:32
	13:55:41	13:55:52	13:56:00	13:56:06	13:56:11
	13:56:15	13:56:20	13:56:27	13:56:35	13:56:52
RUN 9-2	13:57:04	13:57:11	13:57:22	13:57:55	13:58:05
	13:58:28	13:58:39	13:58:46	13:58:54	13:59:01
	13:59:09	13:59:16	13:59:37	13:59:49	13:59:56
	14:00:00	14:00:05	14:00:11	14:00:40	14:00:48
	14:00:57	14:01:10	14:01:19	14:01:28	14:01:37
	14:01:51	14:02:14	14:02:22	14:02:32	
ROLL NUMBER 13	14:37:48	14:38:56	14:39:08	14:39:15	14:39:21
	14:39:46	14:39:58	14:40:12	14:40:41	14:40:48
	14:40:56	14:41:07	14:41:35	14:41:40	14:41:48
	14:42:13	14:42:19	14:42:26	14:42:37	14:43:18
	14:43:24	14:43:42	14:43:48	14:44:05	14:44:11
RUN 9-3	14:44:25	14:44:31	14:44:37	14:45:27	14:45:34
	14:46:05	14:46:10	14:46:16	14:46:21	14:46:26
	14:48:50	14:49:00	14:49:05	14:49:18	14:46:30
	14:46:35	14:46:40	14:46:49	14:46:55	14:47:02
	14:47:09	14:47:15	14:47:21	14:47:26	14:47:40
	14:47:45	14:47:55	14:48:00	14:48:07	14:48:12
	14:48:18	14:48:26	14:48:33	14:48:42	14:49:35
	14:49:44	14:49:51	14:50:01	14:50:07	14:50:16
	14:50:27	14:50:36	14:51:03	14:51:08	14:51:13
	14:51:21	14:51:36	14:51:41	14:51:47	14:51:56
	14:52:05	14:52:38	14:52:44		

**END**

**FILMED**

**7-85**

**DTIC**